

# Technical University of Crete

School of Electronic and Computer Engineering  
Laboratory of Electric Circuits and Renewable Energy Sources

---



## Master Thesis

**Design Optimization of an Electric Energy Production System for  
Power-Supplying the Nodes of Wireless Sensor Networks**

**Mandourarakis Ioannis**

Examination Committee:

**Eftichios Koutroulis, Assistant Professor (Supervisor)**

**Kalaitzakis Kostas, Professor**

**Stavrakakis George, Professor**

**2015**



## **Acknowledgment**

This work was supported by the SYN11-6-925 AquaNet project which is executed within the framework of the “Cooperation 2011” program of the Greek General Secretariat for Research & Technology (GSRT), funded through European Union and national funds. I would like to thank the Municipal Enterprise for Water and Sewage of the city of Chania (Greece) for their contribution during the experimental performance evaluation processes and “Georgios Liontas & Co. E.E.” (Katerini, Greece) for their contribution in the development of the experimental prototype systems, as well as the administration and technical personnel of the Telecommunication Systems Research Institute (Technical University of Crete, Greece) for their assistance in conducting this research.

Also, I would like to express my gratitude to my supervisor Prof. Eftichis Koutroulis for the useful comments, remarks and engagement through the learning process of this master thesis. Furthermore I would like to thank Antonios Igglezakis for introducing me to some useful coding tactics, as well as Kostas Loizou for the back-logging support on the way. Lastly, I would like to thank Juliana P. H. Sanches for her assistance in proof-reading the text of this thesis, as well as my loved ones, who have supported me throughout the entire process, both by keeping me harmonious and helping me putting pieces together.

I will be grateful forever for all your love.

Chania, February 2015



## **Abstract**

The widespread utilization of the Wireless Sensor Networks (WSNs) that are power-supplied by Renewable Energy Sources (RES) is now leading scientific research towards the development of innovative sizing optimization techniques and configurations that aim in the service of multi-criteria objectives of economical and/or technical nature. The most frequently used ones have to do with the minimization of the overall cost and the maximization of the overall system efficiency, in terms of energy redundancy and operational reliability. Sizing optimization techniques are being introduced, where there is a tradeoff amongst similar to the aforementioned criteria that often contradict to each other (e.g. reliability is improved when economical cost or energy redundancy are increased).

In this thesis, two complementary design optimization methods (a circuit-level and a system-level study) are presented for deriving the optimal configuration of the RES-based energy production system of a WSN node, such that its total lifetime cost is minimized, while simultaneously guaranteeing that the data-acquisition equipment is uninterruptedly power-supplied during the entire year. The experimental results verify that, by applying the design variables as they were derived by the proposed optimization techniques at both the circuit and the system level, RES-based power-supply structures with a lower lifetime cost and higher power-processing efficiency are derived, compared to the non-optimally designed configurations. The design optimization and experimental results indicate that by using the proposed techniques, the total cost of the RES-based power supply system is reduced by 15.7 % and the DC-DC converter efficiency is increased by 5.5 % compared to the corresponding results obtained by non-optimized power-supply structures.

## **Publications**

A part of the work which is presented in this thesis has been accepted for presentation at the 2015 IEEE International Conference on Industrial Technology (Seville, Spain, 17-19 March 2015) as the following paper: *I. Mandourarakis and E. Koutroulis, "Optimal Design of a Boost-type DC-DC Converter for PV Power-Supplied Wireless Sensor Networks"*.

Keywords : Renewable Energy Sources, Genetic Algorithms, Wireless Sensor Networks, power supply, sizing optimization, DC-DC converter, efficiency, LCOE

**TABLE OF CONTENTS**

<b>1. Introduction.....</b>	<b>2</b>
<b>2. Modeling and Design Optimization.....</b>	<b>8</b>
<b>2.1. DC-DC Converter .....</b>	<b>8</b>
<b>2.1.1. Circuit Modeling and Proposed Approach.....</b>	<b>8</b>
<b>2.1.2. Genetic Algorithms .....</b>	<b>16</b>
<b>2.1.3. Power Loss Distribution .....</b>	<b>20</b>
<b>2.2. RES-based Power Supply .....</b>	<b>23</b>
<b>2.2.1. Proposed Optimization Method.....</b>	<b>24</b>
<b>2.2.2. Optimal Sizing Concept and Equations.....</b>	<b>24</b>
<b>2.2.3. Input Data and Constraints .....</b>	<b>26</b>
<b>3. Design Optimization and Simulation Results.....</b>	<b>29</b>
<b>3.1. Circuit-level optimization.....</b>	<b>29</b>
<b>3.2. System-level optimization.....</b>	<b>36</b>
<b>4. Prototype Implementation .....</b>	<b>41</b>
<b>4.1. Development of the energy management unit .....</b>	<b>48</b>
<b>5. Experimental results .....</b>	<b>68</b>
<b>5.1. Circuit-level optimization.....</b>	<b>68</b>
<b>5.2. System-level optimization.....</b>	<b>73</b>
<b>6. Conclusion .....</b>	<b>76</b>
<b>7. References .....</b>	<b>78</b>



# 1. Introduction

The installation of Wireless Sensor Networks (WSNs) has been increased during the last years, since they enable the measurement of multiple parameters of interest (e.g. meteorological conditions, operational parameters in buildings and industrial environments etc.) over distributed areas [1]. Frequently the sensing nodes of WSNs are distributed over geographically isolated areas, where there is lack of access to electricity. Thus, the WSN nodes, comprising sensors and data-acquisition devices, are power-supplied by Renewable Energy Sources (RES), such as Photovoltaics (PVs) and Wind-Generators (W/Gs), and the RES-generated power is interfaced through chargers (usually DC-DC converters) to storage devices (usually sealed lead-acid or lithium/polymer batteries) [2] and the electric load (e.g. data-acquisition devices, wireless transmitters etc.). The optimal sizing of the RES-based power production units, in order to minimize the cost of the WSN energy production system and simultaneously guarantee that the load energy requirements are covered, is of great importance.

As far as it concerns the optimal sizing of RES systems, various design techniques have been proposed in the scientific literature. The driving force that leads to these design concepts is the fact that the environmental conditions (i.e. solar irradiation, ambient temperature and wind speed), as well as the market prices of the balance-of-system devices differ from place to place around the globe and, additionally, the load energy requirements depend on the target application. These facts render the calculation of the optimal solution in terms of the power capacity of the RES units, as a new challenge for every single case under study.

In [3], a sizing methodology for stand-alone PV systems based on the Particle Swarm Optimization (PSO) algorithm is presented. The Annualized Reliability and Cost of System (ARCS) is used as an objective function of the optimization process, which includes the

concepts of Expected-Energy-Not-Supplied (EENS) and Expected-Excessive-Energy-Supplied (EEES). In [4], multi-criteria optimization of a hybrid system is performed by employing the elitist Non-Dominated sorting Genetic Algorithm (NSGA-II), which belongs to the class of multi-objective evolutionary algorithms [5]. In [6], Genetic Algorithms (GAs) are used to detect the optimal size of a PV array for power-supplying a critical load, with the minimum CAPital EXpenditure (CAPEX) and OPerational EXpenditure (OPEX), respectively, while simultaneously achieving the desired Loss of Power Supply Probability (LPSP). The GAs are favorable in such problems, since they are computationally efficient. Two more applications of GAs are presented in [7] and [8], respectively, where the capacity of a PV source and battery bank, as well as the PV-generator tilt angle have been employed as decision (i.e. design) variables, while the investment and maintenance costs have also been taken into account during the optimization procedure. GAs are also applied in [9], which focuses on the design of stand-alone hybrid RES systems using a multi-criteria analysis method for minimizing various system cost metrics, such as the capital, operation and maintenance costs. Similarly, [10-12] aim at the sizing optimization of hybrid RES systems by focusing on the minimization of the total cost of the energy-production system and the maximization of its reliability. In all of these cases, the optimization process is accomplished by using technical and economic simulation models, which are available in the HOMER software [13].

The optimal sizing of a PV/wind/diesel hybrid energy system using daily-averaged meteorological data is presented in [14]. A method for the optimization of a wind/PV/diesel system is proposed in [15], where the minimization of CO<sub>2</sub> emissions is also taken into consideration. The sizing optimization of grid-connected hybrid systems is explored in [16] and [17] by focusing on the reduction of power loss and multi-objective optimization criteria, respectively. An approach of energy management in hybrid renewable generation and energy storage systems is presented in [18]. It uses a Fuzzy C-Means (FCM) algorithm for grouping

data of the meteorological conditions at the installation site into clusters of days with similar data points, in order to account for the seasonal variations. Then, GAs are employed for obtaining the optimal energy generation and storage capacities. It has been demonstrated that the flexibility of time-shifting the operation of an electric load, in order to minimize the cost of the power-generation system and maximize its efficiency, depends on a compromise, which must be performed, between the risk of failing to meet the load power demand and a potential reduction of the power-generation system cost. The GA-based optimization of a hybrid topology of a stand-alone RES system, which is comprised of a PV source and a W/G, is presented in [19]. The effect of temporal sampling of the PV source power-production data is examined by comparing the performance of a system optimized using data of high temporal resolution with that of a system optimized using data of lower resolution. It is concluded that by applying a higher sampling rate, solutions closer to the real optimum can be obtained. In [20], the total number of battery replacements (BRPs) is minimized by using a battery cycle-life model in combination with a generalized curve of the relationship between the normalized PV array and battery capacities. This technique has the advantage that the amount of data of the prevailing meteorological conditions, which are required for designing the PV system, is reduced. Thus, this technique is useful in all of those cases where inability to collect such information arises.

The designer must also perform the appropriate decisions in order to address possible issues that may arise in special circumstances where the thermal flow, temperature distribution and electromagnetic interference (EMI) deserve extra care. An example of thermal and EMI modeling and analysis is given in [21]. In [22], the trade-off between accuracy and computation time is explored for producing a dedicated optimization tool, by focusing on the converter performance in terms of the power conversion efficiency, EMI and thermal profile. Optimization techniques have been widely applied for improving the performance of

automotive control systems [23, 24], reactive power flow [25-27], DC/AC inverters of Photovoltaic (PV) systems [28-30], etc. Regarding component sizing of DC-DC converters for power loss optimization, only a few studies have taken place with [23, 24, 31, 32] mainly focusing on the minimization of the volume and cost of an automotive Buck-type DC-DC converter and [33] focusing on the low cost of the prototypes.

The DC-DC converters employed in PV power processing systems, such as those implemented for power-supplying the nodes of a WSN, are required to operate under continuously variable DC input power conditions. Thus, they should be able to optimally exploit the available RES energy for minimizing the total cost of the required RES and energy-storage units, as well as for maximizing the reliability of the overall power-supply system in order to ensure an uninterrupted operation of the WSN node.

The past-proposed design methods of RES systems have been developed for energy production systems with a relatively high power capacity. However, to the authors' knowledge, no study has yet been carried out investigating the design optimization of a stand-alone RES system, which is intended to cover a rather small power consumption, such as that of the electronic devices (e.g. sensors, data-acquisition systems, wireless transceivers etc.) comprised by the nodes of a WSN by considering annual time-series profiles.

The aforementioned concepts mainly refer to the state-of-the-art information found in the modern literature regarding the scientific research and applied techniques used as far as it concerns the optimal sizing design on a system-level. But, as it turns out, there is more ground to cover by firstly (or simultaneously, depending on the research process priorities) focusing on the circuit-level sizing optimization. This can be done by referring to the power-electronics design, which for a RES system mainly focuses on the charger device, which in turn is a DC-DC converter. So, as far as it concerns the circuit of a DC-DC converter, various

operational parameters must be considered in order to ensure that the desired performance is achieved, such as the power conversion efficiency, power density, cost, reliability etc.

In this thesis both aforementioned sizing optimization approaches are being studied. Regarding the circuit-level approach, the method presented is describing the steps for optimally designing the circuit of a Boost-type DC-DC power converter employed in the energy-processing system of a WSN node, which is power-supplied by a PV or W/G source. The target of the proposed method is to derive the optimal switching frequency and values of the components comprising the circuit of a PV power-supplied Boost-type converter, which result in optimal operation in terms of performance metrics such as the power loss at maximum output power, total power loss during the year and Levelized Cost Of the Electricity generated (LCOE) [34]. In more detail, this approach is carried out in two main steps. The first step consists on developing the generalized energy loss models for the four most prevalent power supply components: semiconductor switches (MOSFETs), Schottky diodes, inductors and capacitors. This is done in relation to their driving conditions in terms of the switching frequency they run on. The second step is based on minimizing the power losses and subsequently the cost of energy of the selected architecture by means of Genetic Algorithms (GA). The definition of the respective objective function was formed, while considering the multi-physic constraints imposed by the nature of the problem in relation to the specifications of the field of application. The developed optimization procedure has been validated by numerical simulation and experimental measurements. GA-based techniques are introduced in order to overcome any challenges that the non-linear, stochastic principles involved can hold, while reducing the overall required computational effort. The objective functions have been set to express a multi-criteria problem statement by using a mix of rules defined both in discrete and continuous space. This requirement appears as the design variables concern the representation of distinguished-value lumped electronic components, as well as the narrow

range of sequential values of neighboring operating points (switching frequency). This mix of rules also comes as a benefit that offers a practical advantage in terms of service time when the expert is called to relax any given preset specifications about the extracted by the genetic algorithms outcome (i.e. power loss, cost or combination of both) in order to choose from a narrow range of suitable locally optimal solutions. The resulting circuit that was produced by this approach was assembled using commercial off-the-shelf components and was experimentally tested in various conditions. It passed all stress tests both in the laboratory and in real-world scenarios. The experimental results serve as proof of concept where the optimized solution is being compared to a non-optimized one.

As far as in concerns the system-level optimization, the approach presented is describing the steps for optimally designing the RES-based power supply system of a stand-alone WSN node (i.e. enables to calculate the optimal combination of type and number of the solar cells or wind generators, type and number of the batteries and/or super-capacitors, the PV slope angle and the W/G height of installation), such that its total capital and lifetime maintenance cost is minimized, while, simultaneously, the energy requirements of the electric load during the entire year are completely satisfied. The proposed technique also takes into account the stochastic variability of the meteorological conditions at the installation site, which affects the corresponding RES energy production.

The simulation and experimental results verify the superiority of the RES-based power-supply system of a WSN node, which has been optimally designed using the proposed technique, compared to non-optimized configurations. The same goes for the optimized DC-DC converter circuit design which exhibits superior performance compared to the non-optimized DC-DC converters, when both operate under the same meteorological conditions.

## 2. Modeling and Design Optimization

### 2.1. DC-DC Converter

#### 2.1.1. Circuit Modeling and Proposed Approach

In order to achieve energy independence, each wireless node is power-supplied by small solar panels (PV) or a wind generator (W/G) depending on the availability of solar and wind power in the field of installation. The diagram of Fig. 1 includes, inter alia, the general form of the energy management system that ensures the smooth operation of the nodes' load regardless of the weather conditions. In the scheme of Fig. 1 the Boost converter acts as a battery charger. The circuit that mediates between the PV or W/G components and the electric load is a DC-DC converter of a suitable topology. The topology of the converter is being determined by the voltage ranges specified on its input and output. The one namely used in this thesis is a Step-Up (Voltage Boost) converter.

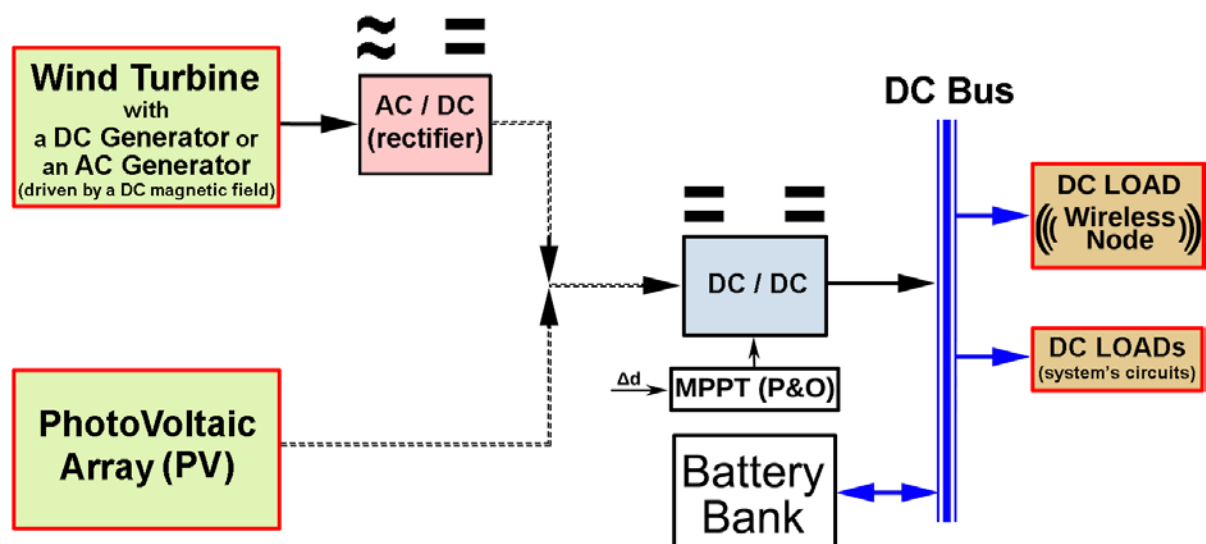


**Fig. 1.** Generalized block diagram of the RES-based power-supply and energy management system for WSN nodes.

The output voltage of the battery load was considered to fluctuate between 11 V and 14.8 V in normal operating conditions. As the input voltage of the PV array could be anywhere between the limits of 0 V and 14.8 V this range was initially used in the control simulations and the integrated circuits of the prototype board. In a Boost converter there are two conduction modes that can be considered, Discontinuous Conductions Mode (DCM) where the inductor's current reaches zero and Continuous Conduction Mode (CCM) where inductor's current is always positive. In this study only CCM was taken into account. The study begins with the identification of the electric components that play a dominant role in the power losses and cost of the circuit. These components are the MOSFET switch, the main reverse diode, the inductor and the output capacitor. Table 1 holds the symbols and a brief description, as well as a typical value range of the design variables and constants associated with the description of the properties and the role of the electronic components as depicted in Fig. 2.

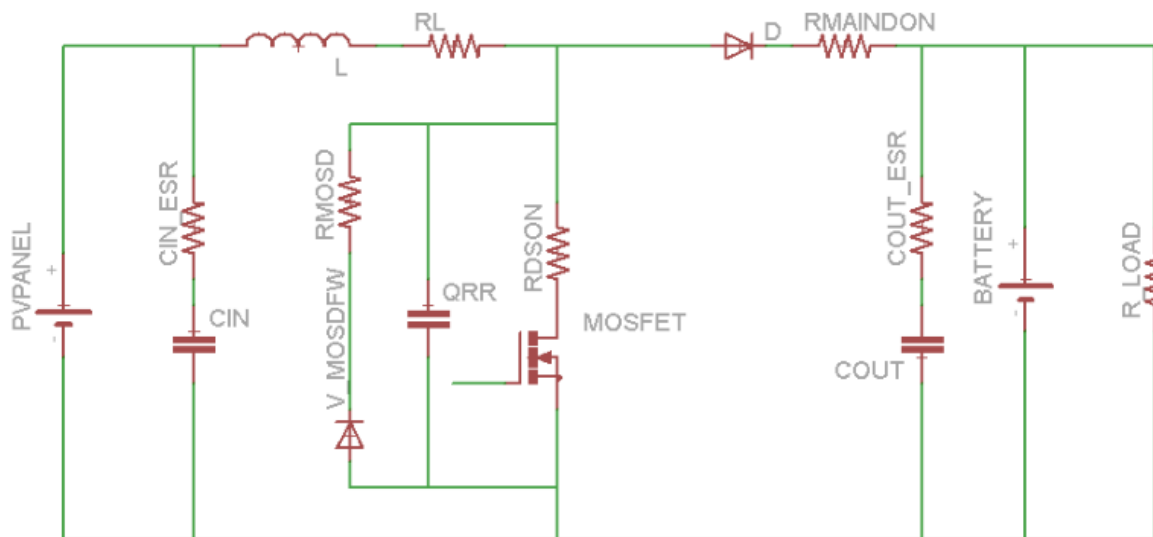


**Fig. 2.** An equivalent circuit of a Boost-type DC-DC Boost Converter for calculating the operation parameters (i.e. design variables, constants and the corresponding power losses) and model equations.

**Table 1.** Boost DC-DC converter power loss model parameters.

<i>Type</i>	<i>Description</i>
$L$	main inductance - based on $I_{out}$ ripple specs
$C_{out}$	output filter capacitance - based on $V_{out}$ ripple specs
$f_s$	switching frequency
$MF_{Count}$	Number of MOSFETs in parallel
$RL_{ESR_{DC}}$	inductor DC resistance
$RL_{ESR_{AC}}$	inductor AC resistance
$C_{outESR}$	output capacitor Equivalent Series Resistance
$R_{MainD_{ON}}$	Resistance of main diode when conducting (ON)
$V_{MainD}$	Forward character of main reverse diode
$R_{MOSD_{FW}}$	resistance of <b>MOSFET</b> flywheel diode when conducting (ON)
$V_{MOSD_{FW}}$	Forward character of <b>MOSFET</b> reverse (flywheel) diode
$V_{MOSDS}$	Forward character of <b>MOSFET</b> Drain-Source junction (ON)
$R_{DS_{ON}}$	resistance of <b>MOSFET</b> drain-source channel when conducting (ON)
$Q_{rr}$	<b>MOSFET</b> reverse recovery charge
$t_{rr}$	<b>MOSFET</b> reverse recovery time
$t_r$	<b>MOSFET</b> switch rise time
$t_f$	<b>MOSFET</b> switch fall time
$V_{Battery}$	Charged battery voltage (may vary later on)
$C_{inESR}$	input capacitor Equivalent Series Resistance
$C_{in}$	input filter capacitance
$R_{Load}$	resistance of output load
$K_I$	Steinmetz equation coefficient
$V_e$	Volume of the inductor core

To achieve energy independence, the WSN node is powered by one or more PV modules. Fig. 1 presents the block diagram that illustrates the channeling of the generated power to be managed by the power processing system of a WSN node. In this scheme, either a PV or a W/G may be used, depending on the availability of solar and wind power in the field of installation. A battery bank stores the surplus of the PV-generated energy and a special designed microprocessor-based controlling unit is typically used to regulate the DC-DC converter, implementing Maximum Power Point Tracking (MPPT) and battery-charging

operations [35, 36]. Some useful generic equations are shown in Table 2 for reference purposes. On the other hand, Table 3 shows power-loss equations specific to the circuit that this study focuses on, that are being used in the simulation code of the respective mathematical models [36-43].

**Table 2.** Useful reference equations for a boost-type DC-DC converter.

<b>Voltages Ratio</b>	$M(D) = \frac{V_{out}}{V_{in}} = \frac{1}{1-D}$	<b>Duty Cycle (no losses)</b>	$D = 1 - \frac{V_{in}}{V_{out}} = \frac{V_{out} - V_{in}}{V_{out}}$
<b>Output Voltage Drop (DC losses)</b>	$V_{out} = \frac{V_{in} - I_L \cdot RL_{ESR_{DC}}}{1-D} - V_{MainD} - V_{MOSDS} \cdot \frac{D}{1-D}$	<b>Duty Cycle (estimation)</b>	$D = \frac{V_{out} - V_{in} + V_{MainD} + I_L \cdot RL_{ESR_{DC}}}{V_{out} + V_{MainD} - V_{MOSDS}}$
<b>Power Input</b>	$P_{in} = P_{MPPT\_PV(SERIES)}$	<b>Input Voltage</b>	$V_{in} = V_{MPPT\_PV(SERIES)}$
<b>Output Voltage</b>	$V_{out} = V_{battery}$	<b>Input Current</b>	$I_{in} = P_{in} / V_{in}$
<b>Inductor Current (average)</b>	$I_{L_{AVG}} = I_{in}$	<b>Input Current (no loss estimation)</b>	$I_{in} = \frac{I_{out}}{1-D}$
<b>Power Balance</b>	$P_{in} = P_{out} + P_{Losses}$		
<b>Power Losses</b>	$P_{SUM\ Losses} = P_{Inductor} + P_{Diode} + P_{Cout} + P_{MOSFET}$		
<b>Output Ripple Current</b>	$di = \frac{D \cdot V_{in}}{L \cdot f_s}$	<b>Inductor Minimum Current - MOSFET ON</b>	$di_{ON} = I_{L_{AVG}} - \frac{di}{2}$ (also called "I offset")
<b>Output Ripple Voltage</b>	$dv = \frac{D \cdot V_{out}}{R_{Load} \cdot C_{out} \cdot f_s}$	<b>Inductor Maximum Current - MOSFET OFF</b>	$di_{OFF} = I_{L_{AVG}} + \frac{di}{2}$

The equivalent circuit of the Boost-type is depicted in Fig. 2. The parasitic components, which affect the power loss of the DC-DC converter (i.e.  $r_{c,in} = r_L = r_{ds}$  etc.) are also included in that circuit. Multiple power MOSFETs may be connected in parallel, depending on the power-loss and manufacturing cost requirements and they are typically controlled, through a gate-drive circuit, according to the Pulse Width Modulation (PWM) technique. The components playing a dominant role in the power losses and cost of the circuit are the

MOSFET switch(es), the power diode, the inductor and the output capacitor. Their electrical characteristics, together with the value of the switching frequency of the DC-DC converter PWM control signal, shape the power-consumption behavior of the overall Boost-type DC-DC converter.

**Table 3.** Main power loss equations for the DC-DC converter circuit.

<b>Inductor DC Losses</b>	$P_{L_{DC} \text{ Losses}} = R_{L,ESR_{DC}} \cdot I_{L_{DCavg}}^2, \quad R_{L,ESR_{DC}} \text{ is a function of } L$ $I_{L_{DCavg}} = I_{L_{AVG}} = I_{in} = \frac{I_{out}}{1-D}$	
<b>Inductor AC Losses</b>	$P_{L_{AC} \text{ Losses}} = R_{L,ESR_{AC}} \cdot I_{L_{ACrms}}^2, \quad R_{L,ESR_{AC}} \text{ is a function of } L, f_s$ $I_{L_{ACrms}} = \frac{di}{\sqrt{3}} \text{ (RMS of any triangle shape function : } I_{rms_{TRIANGLE}} = \frac{\text{peak value}}{\sqrt{3}})$	
<b>Inductor Core Losses</b>	$P_{L_{CORE} \text{ Losses}} = \frac{1}{2} \cdot K_I \cdot f^x \cdot B^y \cdot V_e$ <p>The product <math>f^x \times B^y = g(f_s)</math> is given by a graph and calculated using the "Piecewise Cubic Hermite Interpolating Polynomial" of Matlab environment. The term <math>\frac{1}{2}</math> is added according to the 'Power Design' directions of <a href="http://www.mag-inc.com/">http://www.mag-inc.com/</a></p>	(1)
<b>Inductor Losses</b>	$P_{Inductor} = P_{L_{DC} \text{ Losses}} + P_{L_{AC} \text{ Losses}} + P_{L_{CORE} \text{ Losses}}$	(2)
<b>Diode Losses</b>	$P_{Diode} = V_{MainD} \cdot I_{D_{AVG}} + R_{MainD_{ON}} \cdot I_{D_{RMS}}^2$ $I_{D_{AVG}} = (1-D) \cdot I_{in} = I_{out}$ $I_{D_{RMS}} = \sqrt{I_{D_{DC}}^2 + I_{D_{AC}}^2}, \quad I_{D_{DC}} = di_{ON} \cdot \sqrt{D},$ $I_{D_{AC}} = di \cdot \sqrt{\frac{(1-D)}{3}}$	(3)
<b>Output Capacitor Losses</b>	$P_{C_{out}} = I_{C_{out}}^2 \cdot C_{outESR}, \quad C_{outESR} \text{ is a function of } C_{out}$ $I_{C_{out}} = I_{out} \cdot \sqrt{\frac{D}{1-D}}$	(4)
<b>MOSFET Conduction Losses</b>	$MF_{CM \text{ Losses}} = I_{DS \text{ RMS}}^2 \cdot R_{DS_{ON}}$ $I_{DS \text{ RMS}} = \sqrt{D} \cdot I_{in} / MF_{Count}$	
<b>MOSFET Switching Losses</b>	$MF_{SW \text{ Losses}} = (Energy_{ON} + Energy_{OFF}) \cdot f_s$ $Energy_{ON} = V_{dd} \cdot (di_{ON} / MF_{Count}) \cdot \frac{(t_r + t_f)}{2} + Q_{rr} \cdot V_{dd},$ $V_{dd} = V_{in} \quad Energy_{OFF} = V_{dd} \cdot (di_{OFF} / MF_{Count}) \cdot \frac{(t_r + t_f)}{2},$ $V_{dd} = V_{in}$	

<b>MOSFET's Flywheel Diode Conduction Losses</b>	$FW_{CM_{Losses}} = V_{MOSD_{FW}} \cdot I_{FW_{AVG}} + R_{MOSD_{FW}} \cdot I_{FW_{RMS}}^2$ $I_{FW_{AVG}} = (1-D) \cdot I_{in} / MF_{Count}$ $I_{FW_{RMS}} = \sqrt{(1-D)} \cdot I_{in} / MF_{Count}$	
<b>MOSFET's Flywheel Diode Switching Losses</b>	$FW_{SW_{Losses}} = Energy_{FW_{ON}} \cdot f_s$ $Energy_{FW_{ON}} = \frac{1}{4} \cdot Q_{rr} \cdot V_{drr}, \quad V_{drr} = V_{in} \quad (\text{in worst case scenario})$	
<b>MOSFET Losses</b>	$P_{MOSFET} = MF_{Count} \cdot (MF_{CM_{Losses}} + MF_{SW_{Losses}} + FW_{CM_{Losses}} + FW_{SW_{Losses}})$	(5)

The DC-DC converter is being designed by using the power loss models of the various individual electronic components it is composed of. The aim is to reduce both the manufacturing cost and the charging process power losses, whereas a tradeoff between these two goals keeps challenging the minimization technique which must be employed.

The power loss model and equations of the individual electronic components of the DC-DC converter have already been shown in Tables 1, 2 and 3. The total power loss of the DC-DC power converter is given by the following equation:

$$P_L = P_{MOSFET} + P_{Diode} + P_{Inductor} + P_{Cout} + P_C \quad (6)$$

where  $P_{MOSFET}$ ,  $P_{Diode}$ ,  $P_{Inductor}$ ,  $P_{Cout}$  and  $P_C$  are the power loss of the power MOSFET(s), diode, inductor and output capacitor, respectively, of the DC-DC converter, while  $P_C$  is the total power loss of the input capacitor and control unit, which have been assumed to be constant.

At the first step of the proposed approach, the optimization problem is reduced to the minimization of the power loss equation (6) that consists of four individual equations (except  $P_C$  which has been assumed to be constant), each one of them modeling the power losses of the dominant electronic components as shown in (5) for the MOSFET switch, in (3) for the main reverse diode, in (2) and (1) for the inductor and in (4) for the output capacitor.

The parameters  $V_{MainD}$  and  $R_{MainD}$  correspond to the forward voltage and the conduction resistance of the reverse diode, respectively. The product  $\frac{1}{2} \cdot K_I \cdot f^x \cdot B^y \cdot V_e = g(f)$  in (1) (see Table 3) is a function whose parameters ( $K_I$ ,  $V_e$ ) are being extracted from the inductor's characterization curve that is usually found in the manufacturer's datasheet graphs yielding its "performance factor" in terms of flux density ( $B^y$ ) vs. operating frequency ( $f^x$ ). The factor of  $\frac{1}{2}$  is employed considering that the operation of the inductor will be using in average around half of the usable flux density. The parameter  $K_I$  is Steinmetz equation coefficient and parameter  $V_e$  is the volume of the inductor core.

The equation (5) includes –in order of appearance– the MOSFET switching losses, the MOSFET conduction losses, the switching losses of the MOSFET flying diode and the conduction losses of the MOSFET flying diode.

Similarly, the equation (2) includes –in order of appearance– the conduction (DC) and the ripple (AC) losses in the inductor, as well as the magnetic core losses in it making use of the equation (1), which is a generalization of the Steinmetz equation. The analytical model equations that evaluate the conduction and switching semiconductor losses of the MOSFET and the reverse diode have been composed by the information found in [37-41].

The copper and core losses of the inductor have been composed by the information found in [40-44]. The input filter capacitor losses, the printed circuit tracks conduction losses and any other losses based coming from the operation of the peripheral integrated circuitry were not taken into account. These losses are weak and do not fluctuate a lot so they are considered to be constant. Also, they can be easily approximated with a constant value when required. To overcome the recursive nature of these equations, a first-order zero crossing technique with a repetitive loop was used.

The composition of the analytical equations which are required for calculating the conduction and switching semiconductor losses of the power MOSFET(s) and diode have also been assisted by the information available in [45-47]. Similarly, the calculation of the copper and core losses of the inductor have been assisted by the information available in [47-50].

The parameters of equation (1) are extracted for calculation by using the "Piecewise Cubic Hermite Interpolating Polynomial" of the Mathworks MATLAB environment. This applies also for the correlated parameters of Table 4, which summarizes the relevant information needed to form the respective power loss and cost equations, i.e. the main objectives, the design variables and all correlated parameters whose values are functionally dependent on the design variables.

**Table 4.** Correlated parameters.

<b>Optimization Objective</b>	<b>Symbol</b>	<b>Description and Unit</b>	<b>Function of</b>
<i>Design Variables</i>			
Power Loss and Cost	$MF_{Count}$	MOSFETs in parallel (#)	-
Power Loss	$L$	Reverse Diode inductance (H)	-
Power Loss	$C_{out}$	Output filter capacitance (F)	-
Power Loss	$f_s$	Switching frequency (Hz)	-
<i>Correlated Parameters</i>			
Power Loss	$R_{L,ESR_{DC}}$	Inductor DC resistance (Ohm)	$L$
Power Loss	$R_{L,ESR_{AC}}$	Inductor AC resistance (Ohm)	$L, f_s$
Power Loss	$C_{outESR}$	Output capacitor equivalent series resistance (Ohm)	$C_{out}$
Cost	$C_{outCOST}$	Output filter cost (€)	$C_{out}$
Cost	$C_{inCOST}$	Output filter cost (€)	$C_{in}$
Cost	$L_{COST}$	Inductor cost (€)	$L$

The costs of the MOSFET switch and the diode, as well as the main electrical characteristics of the diode (i.e. the conducting resistance and the forward character of it) are

not included in Table 4. This is an indirect consequence of the nearly fixed market prices of these two active power components in relevance to their electric specifications. The characterization constants of the MOSFET switch, the diode and the inductor can easily be extracted from the manufacturer's datasheets. For the generation of the parameters that are being fed into the functions for the cost evaluation of the passive components, relevant pricing data are available in the international market. The number and electrical characteristics of the passive components, as well as the value of the switching frequency of the overall circuit shape the power consumption behavior of the DC-DC converter under design.

### **2.1.2. Genetic Algorithms**

In the Computer Science field of artificial intelligence, Genetic Algorithms (GAs) are falling under the group of methods of reasoning calculations, which operate as search heuristics that mimic the process of natural selection. More specifically, the GA tools that are used in this thesis belong in the larger class of Evolutionary Algorithms (EAs) whose functions are inspired by techniques such as inheritance, mutation, selection and crossover. GAs serve as excellent tools when it comes to produce good estimations about non-linear or stochastic problems.

Fig. 3 shows the flowchart of the circuit optimization algorithm, which describes the process followed to approach the optimum combination of the electronic components that will comprise the DC-DC converter in design. The objective functions considered by the optimization algorithm are the ones having to do with the cost and the overall reliability of the DC-DC converter circuit.

The GA pictured in Fig. 3 was able to produce the required results with a precision of less than 1 % in a few seconds. In the same computer it was calculated –by projecting the amount of time it needed per loop in simpler executions– that an exhaustive search algorithm that

would produce the same accuracy for the result would need to search for a significantly longer time period. The GA was run for many different objective functions. These include the ones that seek for the combination of the design variables that will reveal the values that minimize the power losses and the ones that minimize the LCOE which is expressed as the total cost of the device divided by the useful power it produces (i.e. the input power minus the power losses).

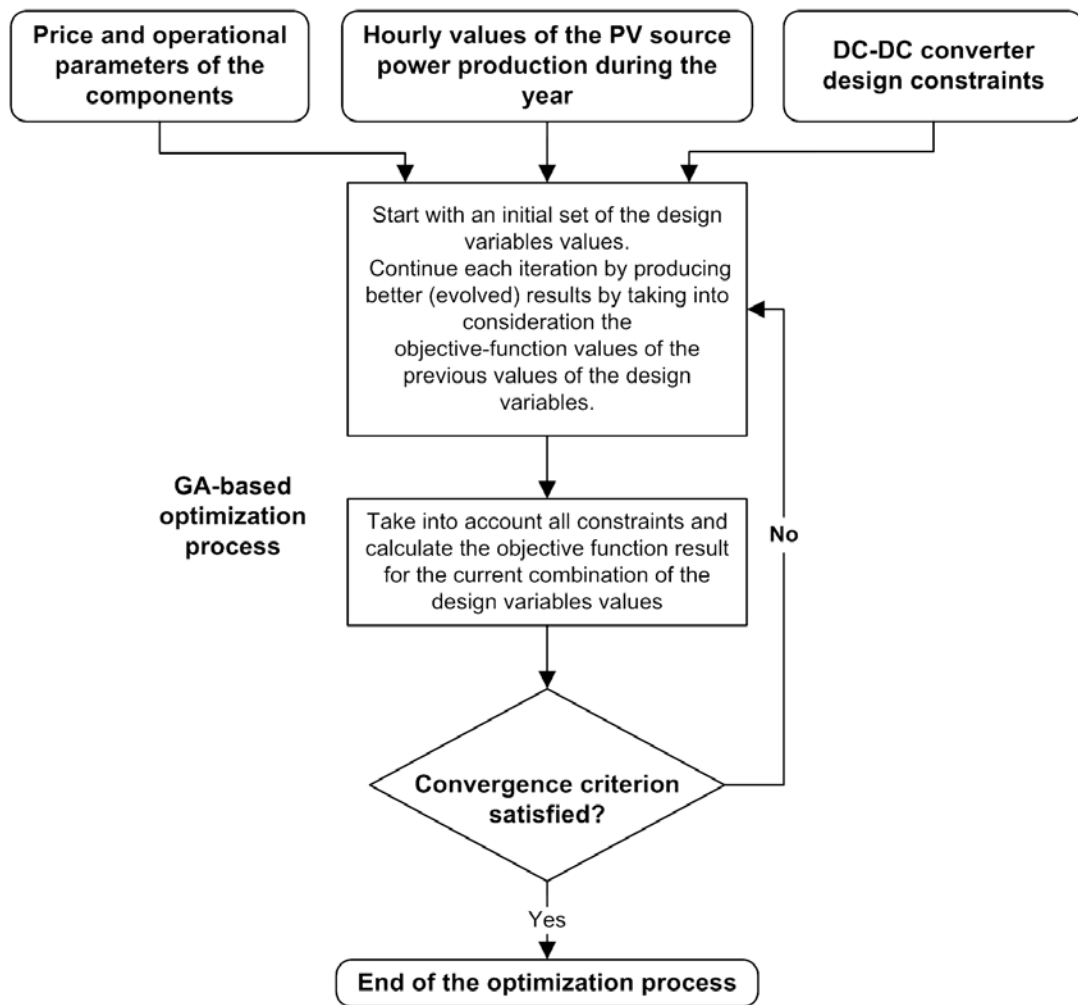


**Fig. 3.** A flowchart of the proposed circuit-level optimization process using GAs.

So, alongside with the aforementioned development of the system sizing optimization algorithm concerning the power supply system as a whole, a development of an additional genetic algorithm took place. This one was specifically aiming to the sizing optimization of

the circuit that is responsible for the power management of the energy produced by the PV or W/G sources, whose type and parameters were chosen by the system-level optimization.

The related code, also written in the MATLAB environment was purely focused to further optimize the design of the electronic circuit of the converter, by taking into consideration a system whose characteristics resulted from the solution of the aforementioned system-level optimization problem. As far as it concerns the design parameters of the circuit-level optimization, these are: type of parts to be used, number of MOSFETs connected in parallel, the capacity of the output capacitor, the inductance of the power converter and the switching frequency. The optimization of the design of the energy management circuit (i.e. the battery charger) ensured the minimization of the cost of the power converter. Also, it minimized the electricity power losses when charging any of the subsystems of the wireless node.

The target of the proposed, circuit-level optimization method is to derive the optimal switching frequency and values of the components comprising the DC-DC converter, so that the desired performance metric of the power converter is optimized. The design variables considered in the optimization process are, again, the switching frequency,  $f_s$ , the number of power MOSFETs connected in parallel,  $MF_{Count}$ , the inductance,  $L$  and the output capacitance  $C_{out}$ . The optimization process is performed for deriving the optimal values of three alternative performance metrics, which correspond to alternative objective functions of the optimization process. The first one maximizes the power converter efficiency under nominal output power conditions. The power conversion efficiency,  $n$ , is given by the following equation:

$$n = \frac{P_o}{P_{PV}} = \frac{P_o}{P_o + P_L} \quad (7)$$

where  $P_{pv}$  is the power produced by the PV source under MPPT conditions and  $P_o$  is the output power of the DC-DC converter.

In order to achieve this target, the minimum value of  $P_L$  is calculated using (10) under the condition that the value of  $P_o$  is equal to the nominal output power of the DC-DC converter.

The second optimization objective is to minimize the total energy loss of the DC-DC converter during the year, which is given by the following equation:

$$E_{L,tot} = \sum_{i=1}^{8760} P_{L,i} \cdot \Delta t \quad (8)$$

where  $P_{L,i}$  is the total power loss of the DC-DC converter at hour  $i$  ( $1 \leq i \leq 8760$ ) and  $\Delta t$  is the time-step which has been set equal to 1 h.

The third alternative target of the proposed optimization process is to minimize the Levelized Cost Of the Electricity generated (  $LCOE$  ), which is calculated as follows:

$$LCOE = \frac{C_m}{E_{tot}} = \frac{C_m}{\sum_{i=1}^{8760} (P_{pv,i} - P_{L,i}) \cdot \Delta t} \quad (9)$$

where  $C_m$  (€) is the total manufacturing cost of the DC-DC converter,  $E_{tot}$  is the total energy transferred to the battery bank and electric load of the WSN node during the year and  $P_{pv,i}$  is the output power of the PV source at hour  $i$  ( $1 \leq i \leq 8760$ ).

The value of  $C_m$  in (9) is equal to the sum of the prices of the individual components comprising the DC-DC converter. The output current of the DC-DC converter,  $I_o$ , which is required for deriving the value of  $P_L$  in (1) and (7)-(9), is calculated for each value of PV-generated power during the year by solving the following power-balance equation:

$$P_{pv} = P_L + V_o \cdot I_o \quad (10)$$

where  $P_{pv}$  is the power produced by the PV source and  $V_o$  is the output voltage of the DC-DC converter. The value of  $P_o$  in (10) is numerically calculated using a properly developed software program, which implements a zero-crossing detection algorithm with a repetitive loop.

The constraints of the circuit optimization process are (likewise in similar studies) mostly based on the maximum levels of the output voltage and current ripples, but can also include (as implemented in this thesis) conditional checks such as for the maximum current that is allowed to run through the MOSFET and the condition of the circuit getting into DCM (these checks in the microcontroller code trigger special frags that can be seen later on in Table 7).

### **2.1.3. Power Loss Distribution**

Looking into the formalization of the problem, this paragraph explains the methods and tools that were used to construct the simulation and model verification tools. The design method that was adopted ensured that a number of constraints were imposed in a way that they could be met by the designated operation of the converter. The algorithms that were developed were able to identify the combination of the components that can present low construction cost and at the same time a very high efficiency in a wide operation range, exactly as it has ideally been defined by the rest of the system's characteristics. In more detail and as it has already been mentioned, at the system level the design variables are the type and the number of PV cells, the angle of PV array slope, the installation height of the W/G as well as the size of the storage devices (battery bank and/or super-capacitors). Fig. 4 presents a screenshot of the analysis of the power losses on the electronic parts in a frequency spectrum.

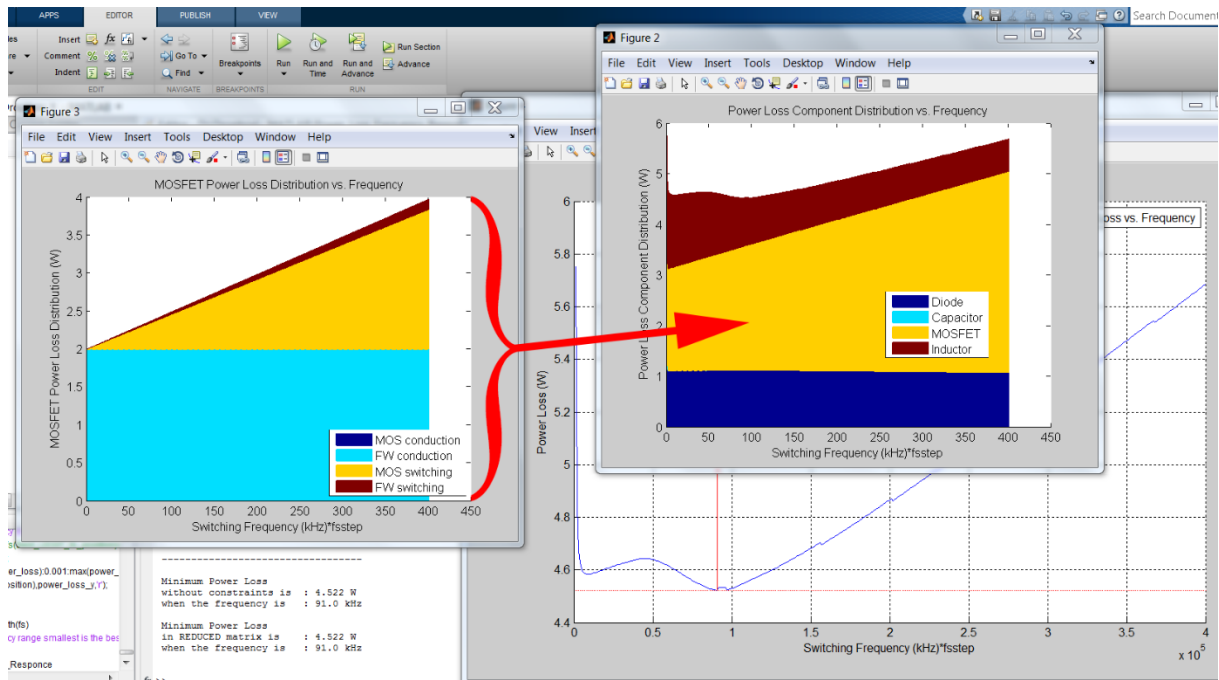


**Fig. 4.** Screenshot of the analysis of the power losses on the electronic parts in various operating frequencies. The aim here is the cross-checking of the GA outcome.

In similar terms like before, the design variables on the circuit level are the type and the number of the power MOSFET, the main diode, the filtering capacitors (both input and output) and the main inductor of the DC-DC converter and extends to physical quantities such as the operating frequency that indirectly affects both cost and type of the above power converter components (and parts as the microprocessor). Also, the developed algorithms examined the extent up to which these components improved or reduced the overall reliability of the circuit and therefore the reliability of the overall power system.

Initially, two design objective functions were employed in the circuit-level optimization process. Specifically it was about the objectives concerning the real-time Power Loss (or efficiency) of the DC-DC converter and its LCOE, which are given by (7) and (9) respectively. The respective calculated optimal values are presented in Table 5. The relative gain of the one case against the other is presented in Table 6. It is observed that the ‘Mean Power Loss’, that is calculated by dividing the sum of all converter’s losses in one year with

the number of hours the year holds, is 3.6 % less than the one presented when the circuit is designed to meet the specifications that lower its LCOE. Likewise, in the case that the LCOE has been chosen as the optimization objective then the ‘Cost of the Electronic Components’ (i.e. the ones actively participating in the pricing ranging) is 15.46 % lower than the one that would be achieved if the same circuit was designed to meet the ‘Power Loss’ objective.

**Table 5.** The calculated optimal values of both objective functions.

<b>Design Variables</b>	<b>Optimization Objectives</b>	
	<i>Efficiency</i> [ in terms of Power Loss / Rated Power]	<i>LCOE</i>
$MF_{Count}$	1	1
$L$	95 $\mu$ H	77 $\mu$ H
$C_{out}$	3000 $\mu$ F	32 $\mu$ F
$f_s$	128.4 kHz	242.3 kHz

**Table 6.** Simulated expectations.

<b>Results Metrics</b>	<b>Optimization Objectives</b>	
	<i>Efficiency</i> [ in terms of Power Loss / Rated Power]	<i>LCOE</i>
<i>Mean Power Loss (W)</i> [ Annual Power Loss / 8760 ]	0.529 W	0.545 W
<i>Cost of the Electronic Components (€)</i>	9.38 €	7.93 €
<i>Percent Optimization</i>	3.63 %	15.46 %

## 2.2. RES-based Power Supply

A block diagram of the WSN node power-supply system is illustrated in Fig. 1. The electric load of the WSN node, which must be successfully power-supplied by the RES-based energy production system under design, comprises the following units: a) one or more sensors for monitoring the parameters of interest (e.g. in the environment, buildings, industries etc.), b) a data-acquisition device for collecting and processing the measurements collected by the sensor(s) and c) a wireless transmission unit for communication with other WSN nodes and/or a central data-collection station. In order to achieve energy autonomy, the WSN node is power-supplied by RES sources. Depending on the solar irradiation or wind potential, which is available at the installation site of the WSN node, the corresponding sensor node is power-supplied by either an array of PV modules, or a W/G. Due to the intermittent nature of solar- and wind-based energy production, an electric energy storage unit, in the form of a battery bank, is integrated in each WSN node in order to power-supply the electronic appliances of the sensor node in case of low solar irradiation or wind speed conditions.

A high-efficiency, switching DC-DC power converter is used to interface the energy produced by the RES source to the battery bank. The operation of the DC-DC power converter is controlled by a microelectronic Energy Management System (EMS), which is implemented using a microcontroller or Digital Signal Processing (DSP) device. The EMS ensures that the maximum power is produced by the RES source, under the stochastically varying meteorological conditions at the installation site, by executing a Maximum Power Point Tracking (MPPT) algorithm [51, 52]. Also, it regulates the battery charging process, such that the recharging time of the battery bank is minimized, by optimally exploiting the RES-generated energy [35].

### 2.2.1. Proposed Optimization Method

With reference to the diagram of the WSN node power-supply system, which is shown in Fig. 1, the target of the proposed design method is to derive, among a list of commercially available PV modules, W/Gs and batteries, the optimal number and type of these units, as well as information regarding their installation parameters (i.e. PV inclination and W/G tower height), such that the lifetime cost of the power-supply system is minimized and simultaneously, the energy requirements of the electric load of the WSN node are completely covered, thus resulting in zero load rejection.

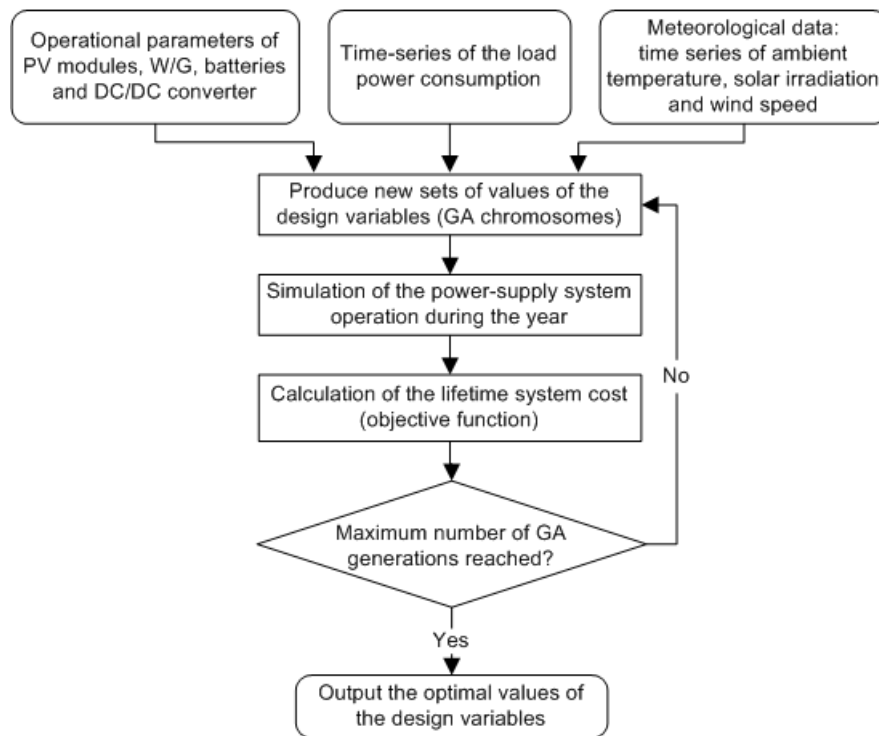


**Fig. 5.** A flowchart of the proposed optimization process.

### 2.2.2. Optimal Sizing Concept and Equations

A flowchart of the proposed design optimization process is shown in Fig. 5. Initially, the designer specifies whether a PV or a W/G power source will be employed for producing the required energy. In the former case, the design variables considered in the optimization process

are the number and tilt angle of the PV modules, the number of PV modules connected in series and parallel, respectively, with the PV array, as well as the rated capacity of the battery bank, which is used as an energy-storage unit. In case that it is selected by the designer to employ a W/G, then the corresponding design variables are the rated power and installation height of the W/G, as well as the capacity of the battery bank.

Also, the designer inputs the following data to the optimization algorithm:

- the time-series of hourly-average values of the meteorological conditions, which prevail at the installation site and
- the operational characteristics of the PV modules (e.g. open-circuit voltage, short-circuit current etc.), W/G (e.g. power-production vs. wind speed curve etc.), DC-DC converter (e.g. curves of efficiency vs. input power etc.) and battery (e.g. nominal capacity, maximum permissible depth of discharge etc.), which will be considered for building the RES system under design, together with their capital and maintenance costs. These operational data are provided by the manufacturer of the corresponding device (e.g. in the device datasheet).

The optimization process is performed by a GA, targeting to derive the optimal values of the aforementioned design variables, which result in the minimization of the total capital and lifetime maintenance cost of the power-supply system,  $C_{PS}$  (€), given by:

$$\text{minimize } \{C_{PS}\} \quad (11)$$

where:

$$C_{PS} = C_{PV} + C_{Chr} + C_{Bat} \quad \text{or} \quad C_{PS} = C_{WT} + C_{Chr} + C_{Bat} \quad (12)$$

and

$$C_{PV} = (C_{PVinvst} + Y \cdot C_{PVmtmc}) \cdot N_{pv} \quad (13)$$

$$C_{WT} = C_{WTinvst} + C_{WTrod} \cdot H_{inst} + Y \cdot C_{WTmntnc} \quad (14)$$

$$C_{Bat} = (C_{BATinvst} + Y \cdot C_{BATmntnc}) \cdot N_{BAT} \quad (15)$$

with  $C_{PV}$  (€) being the total cost of the PV source,  $C_{WT}$  (€) being the cost of the W/G,  $C_{Chr}$  (€) being the cost of the DC-DC converter,  $C_{Bat}$  (€) being the total cost of the battery bank,  $C_{PVinvst}$ ,  $C_{WTinvst}$  and  $C_{BATinvst}$  (€) being the market price of each PV module, W/G and battery respectively,  $C_{PVmntnc}$ ,  $C_{WTmntnc}$  and  $C_{BATmntnc}$  (€/year) being the corresponding yearly maintenance costs,  $Y$  (years) being the planned lifespan of the RES system under design,  $C_{WTrod}$  (€/m) being the cost of the W/G tower per meter of height,  $H_{inst}$  (m) being the W/G installation height, and  $N_{pv}$ ,  $N_{BAT}$  being the total number of PV modules and batteries, respectively, to be used.

### 2.2.3. Input Data and Constraints

During the execution of the optimization process, the GA produces multiple alternative values of the vector of design variables (i.e. chromosomes) [55] and calculates the corresponding values of the total system cost using (12)-(15), according to a set of the RES system devices operational data like the ones illustrated in Fig. 6 . These data are related to the information needed to describe the electrical and economical characteristics of the PVs, W/Gs, the batteries, the DC-DC converter etc. and are usually derived from the respective manufacturer datasheets. The same spreadsheet also holds the time-series related to the environmental (and stochastic) conditions that the system has to face like the solar irradiation, the temperature, the wind speed on the site and the consumption of the load. Then, a simulation of the operation of the RES-based power-supply system during the year is performed with a time step of 1 h, in order to detect whether each vector of design variables produced by the GA satisfies all of the following constraints:

- i. the electric load energy requirements are completely covered during the entire year, in order to obtain a reliable power-supply configuration,
- ii. the stored energy and voltage of the batteries never fall below the minimum permissible limits, which have been specified for the battery under consideration and
- iii. the battery bank State of Charge (SoC) at the end of the year is higher than the initial SoC.

PV_ID	nscs	nscp	NOCT	Pm_STC	Voc_STC	Isc_STC	Kv	Ki	df	delta_i	r_pv	PV_Cst	PV_Mst	
1	20	15	47,50	13,710	10,0600	1,485	-0,0032	0,0008	0,0100	0,0200	0,0036	34,38	6,64	GreenPower
2	20	20	48,00	24,160	12,6800	2,460	-0,0020	0,0042	0,0100	0,0200	0,0036	54,69	5,86	ARTisun
3	20	24	47,50	28,992	12,5600	2,952	-0,0020	0,0042	0,0100	0,0100	0,0036	100,98	5,63	E-Ton Solar T
4	20	20	48,00	24,600	12,7600	2,340	-0,0022	0,0045	0,0100	0,0200	0,0036	40,63	6,25	NEO SOLAR
5	15	35	48,00	30,608	10,7850	2,835	-0,0012	0,0018	0,0100	0,0200	0,0036	56,64	8,50	Panasonic
6	16	30	47,50	32,400	10,0800	2,730	-0,0062	0,0010	0,0100	0,0300	0,0036	82,50	5,63	Spectrolab
7	6	1	47,50	20,700	3,3600	7,000	-0,0032	0,0008	0,0100	0,0200	0,0036	28,13	3,20	greenenergyp
8	8	1	47,50	27,600	4,4800	7,000	-0,0032	0,0008	0,0100	0,0200	0,0036	37,50	3,22	greenenergyp
9	10	1	47,50	34,500	5,6000	7,000	-0,0032	0,0008	0,0100	0,0200	0,0036	46,88	4,15	greenenergyp
10	12	1	47,50	41,400	6,7200	7,000	-0,0032	0,0008	0,0100	0,0200	0,0036	56,25	3,27	greenenergy
11	14	1	47,50	48,300	7,8400	7,000	-0,0032	0,0008	0,0100	0,0200	0,0036	65,63	3,29	greenenergyp
12	16	1	47,50	55,200	8,9600	7,000	-0,0032	0,0008	0,0100	0,0200	0,0036	75,00	3,31	greenenergyp
13	18	1	47,50	62,100	10,0800	7,000	-0,0032	0,0008	0,0100	0,0200	0,0036	84,38	3,34	greenenergyp
14	20	20	47,50	18,280	10,0600	1,980	-0,0032	0,0008	0,0100	0,0200	0,0036	37,50	7,81	GreenPower (
15	20	24	47,50	21,936	10,0600	2,376	-0,0032	0,0008	0,0100	0,0200	0,0036	43,75	11,20	GreenPower (
16	20	28	47,50	25,592	10,0600	2,772	-0,0032	0,0008	0,0100	0,0200	0,0036	50,00	9,69	GreenPower (
17	20	30	47,50	27,420	10,0600	2,970	-0,0032	0,0008	0,0100	0,0200	0,0036	53,13	10,16	GreenPower (
18	20	40	47,50	36,560	10,0600	3,960	-0,0032	0,0008	0,0100	0,0200	0,0036	68,75	12,50	GreenPower (
19	20	50	47,50	45,700	10,0600	4,950	-0,0032	0,0008	0,0100	0,0200	0,0036	84,38	14,84	GreenPower (
20	20	60	47,50	54,840	10,0600	5,940	-0,0032	0,0008	0,0100	0,0200	0,0036	100,00	17,19	GreenPower (

**Fig. 6.** A screenshot of the spreadsheet containing the operational data of multiple alternative types of PV modules, which are input by the designer in the proposed design optimization algorithm.

In case that during the GA evolution process it is detected that any of the design-variables vectors does not fulfill requirements (i)-(iii), then this set of design variables values is rejected, without being considered as a potentially optimal solution of the design optimization problem. In the simulation process, the energy produced by the RES source is initially calculated, using the time-series of meteorological data in combination with appropriate mathematical models of

the devices comprising the RES-based power-supply system [56]. When the RES-generated power is more than that required by the electric load of the WSN node, then the excess energy flows into the battery bank up to the point that it is fully charged, while the remaining power is dropped. In case that the power generation of the RES source is not adequate to cover the load requirements, then the battery bank is discharged accordingly. At each time-step of the simulation process, the energy stored in the battery bank is calculated as follows:

$$E_b(t) = E_b(t-1) + n_b \cdot P_b(t) \cdot \Delta t \quad (16)$$

where  $E_b(t)$  is the energy stored in the battery bank at hour  $t$  of the year (i.e.  $1 \leq t \leq 8760$ ),  $n_b = 81\%$  is the battery round-trip efficiency during charging and  $n_b = 100\%$  during discharging,  $P_b(t)$  is the battery input/output power [i.e.  $P_b(t) < 0$  during discharging and  $P_b(t) > 0$  during charging] and  $\Delta t = 1\text{h}$  is the simulation time-step.

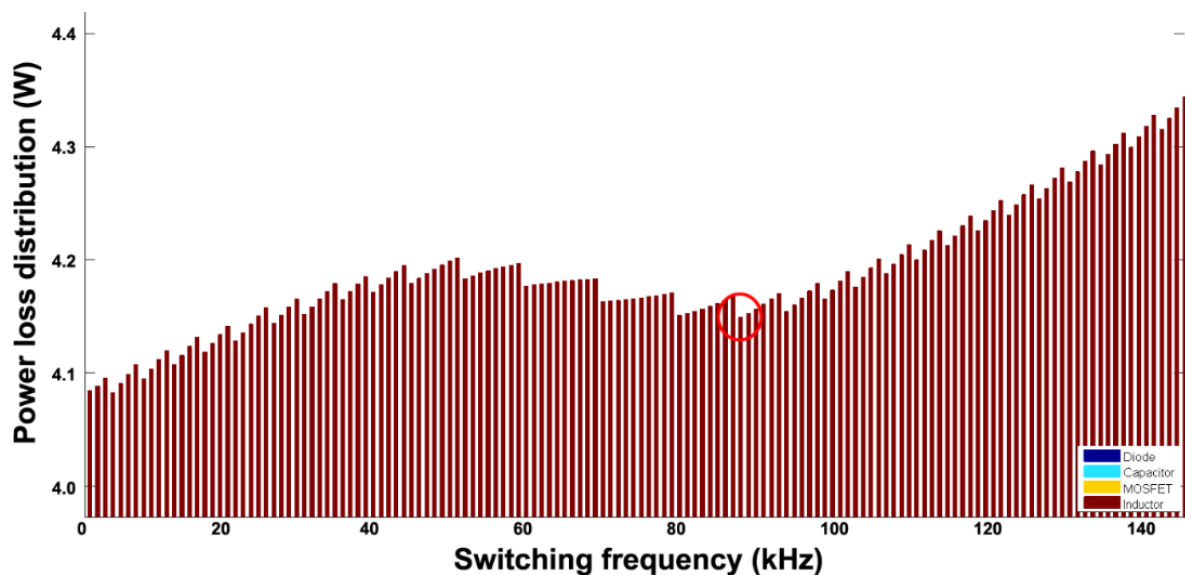
The procedure described above is repeated until a predefined number of GA generations has evolved, each comprising multiple vectors of the design-variables. The set of design variables which results in the minimum value of (12) is considered as the optimum solution. The optimization algorithm depicted in Fig. 5 is repeated for multiple alternative types of PV modules, W/Gs and batteries, which are specified by the designer, in order to derive the optimal lifetime cost and the corresponding optimal configuration of the power-production system for each such combination of device types. Among the individual optimum solutions derived, the overall optimum configuration of the WSN node power-supply system comprises the PV modules, W/G and battery types, which result in the minimum lifetime cost.

Since the power requirements of WSN nodes are typically low (i.e. up to a few tens of Watts), the proposed design method considers that either PVs, or a W/G is employed for power-supplying the WSN node. However, the proposed method can be easily modified for application in hybrid RES configurations too.

### 3. Design Optimization and Simulation Results

#### 3.1. Circuit-level optimization

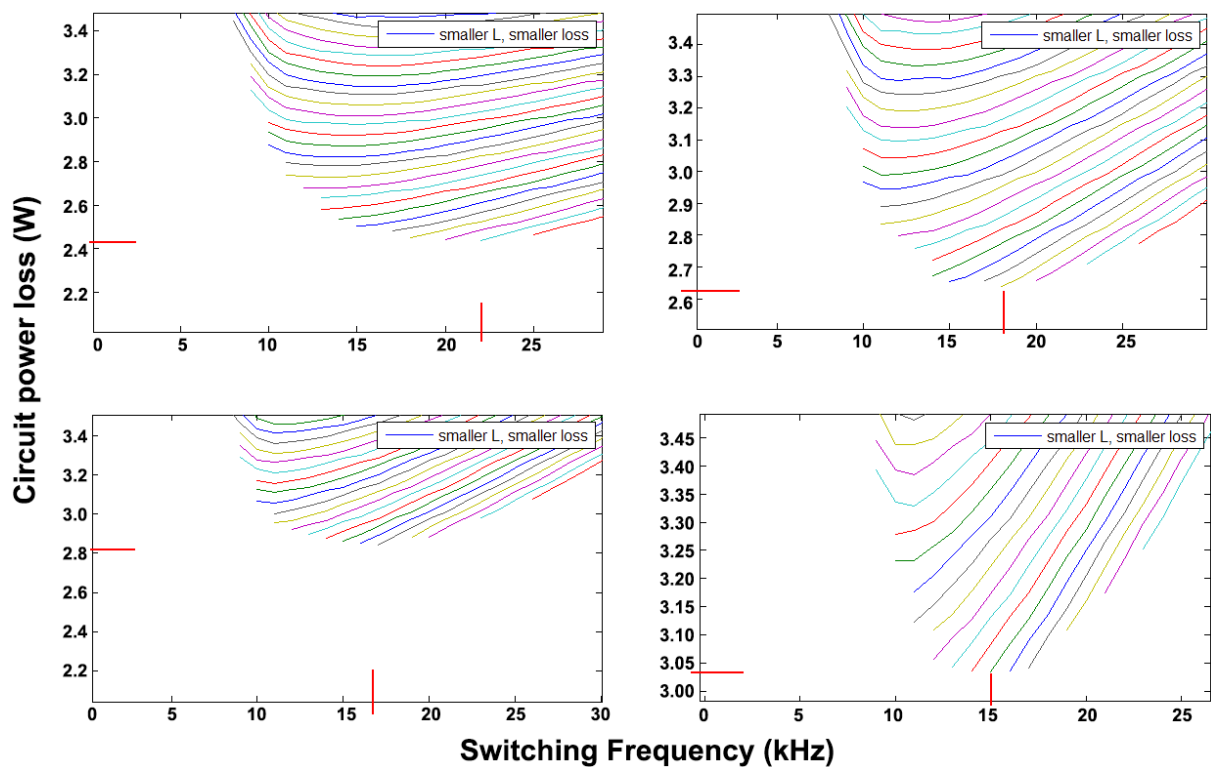
In order to investigate its performance in terms of the total power loss, a Boost-type DC-DC power converter has been considered comprising a 100  $\mu\text{H}$  inductance and operating with a 48 W input power at 6.5 V and 12 V DC input and output voltage levels, respectively. The output current and voltage ripple factors were constrained to be less than 10 %.



**Fig. 7.** Verification of the optimal operating frequency for a given combination (number / type) of components. The power losses of the DC-DC converter are significantly affected by the non-linear losses of the inductor.

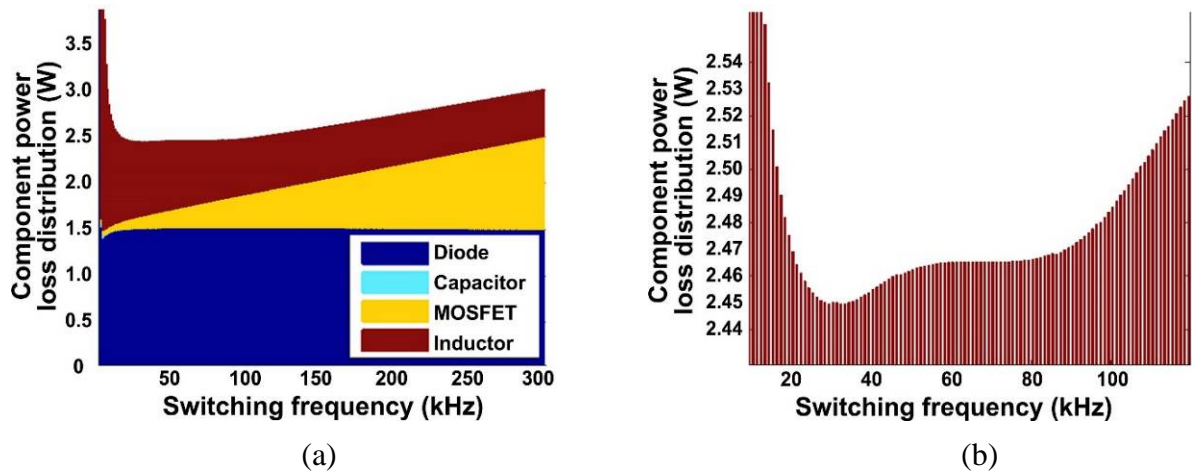
As demonstrated in Fig. 7, the total power loss of the converter exhibits a local minimum at 31 kHz. During the design process of a DC-DC converter, the constraints (at Section 2.1.2) that were imposed by the designer (in order to achieve a more elaborate solution to the optimization problem) happen to shift the optimum operating point from that of the local minimum point.

Fig. 8 depicts four different graphs, each one illustrating the iso-L curves (i.e. the curves where L has a steady value) in relation to the power losses that are developed when the parameter to be changed in each case is the MOSFET number. These graphs reveal useful information about the level of contribution of one of the design variables' (the MOSFET) effect on the objective function's result.



**Fig. 8.** Parametric iso-L curves for the verification of the results as they emerged in different usage scenarios, for the cases of one to four MOSFETs connected in parallel.

One of the ways to depict and focus upon the findings for further research about the factor of each component's influence on the DC-DC converter's overall efficiency over various frequencies, is to graph the power loss contribution graphs. The distribution of total power loss among the dominant (in terms of power loss) components of the DC-DC converter for various switching-frequency values are depicted in Fig. 9.



**Fig. 9.** (a) Power loss distribution among the dominant (in terms of power-loss) components of a Boost-type DC-DC converter for various switching-frequency values and (b) A zoomed-in part of the plot in (a), demonstrating the fluctuation of the overall power loss and its local minimum at 31kHz.

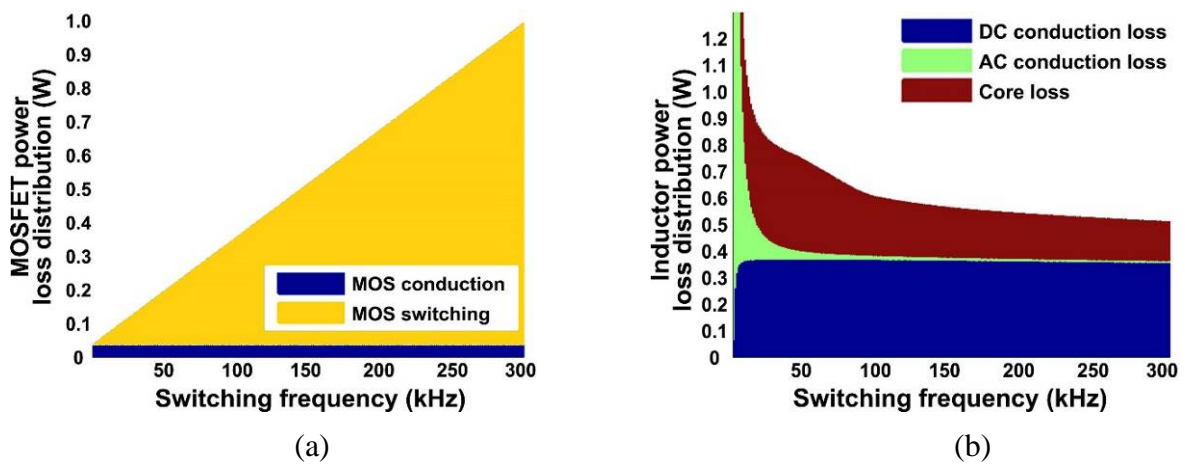


**Fig. 10.** Distribution of power losses in individual components of the Boost-type DC-DC converter: (a) power MOSFET and (b) inductor.

The utilization of the same technique that was used to plot the graphs of Fig. 9 is used to plot the graphs of Fig. 10 where the distribution of the power losses focused in each one of the two major components, the MOSFET switch and the inductor. The distribution of the power losses in the MOSFET switch and power inductor is illustrated in Fig. 10, revealing the scale of influence of each type of losses in the respective components.

From this investigation it is clear that the inductor is the main component that injects non-linear irregularities to the objective function and since similar irregularities are prone to be expected as far as it concerns its pricing and the resulting overall LCOE, the optimization challenge becomes a problem to be solved by the introduction of Genetic Algorithms. In order to prepare the ground for the introduction of Genetic Algorithms, one more clarification is due. The plot of Fig. 11 clarifies the behaviour of the inductor in a tuple of more cases by simulating the power loss vs. frequency distribution for various inductance values. Additional plots, which were generated for up to four MOSFETs connected in parallel (Fig. 8), indicated that the shape of the surface shown in Fig. 11 preserves its monotony while the neighbourhood of the global minimum is moving towards higher losses of about 3% for each additional power MOSFET connected in parallel.

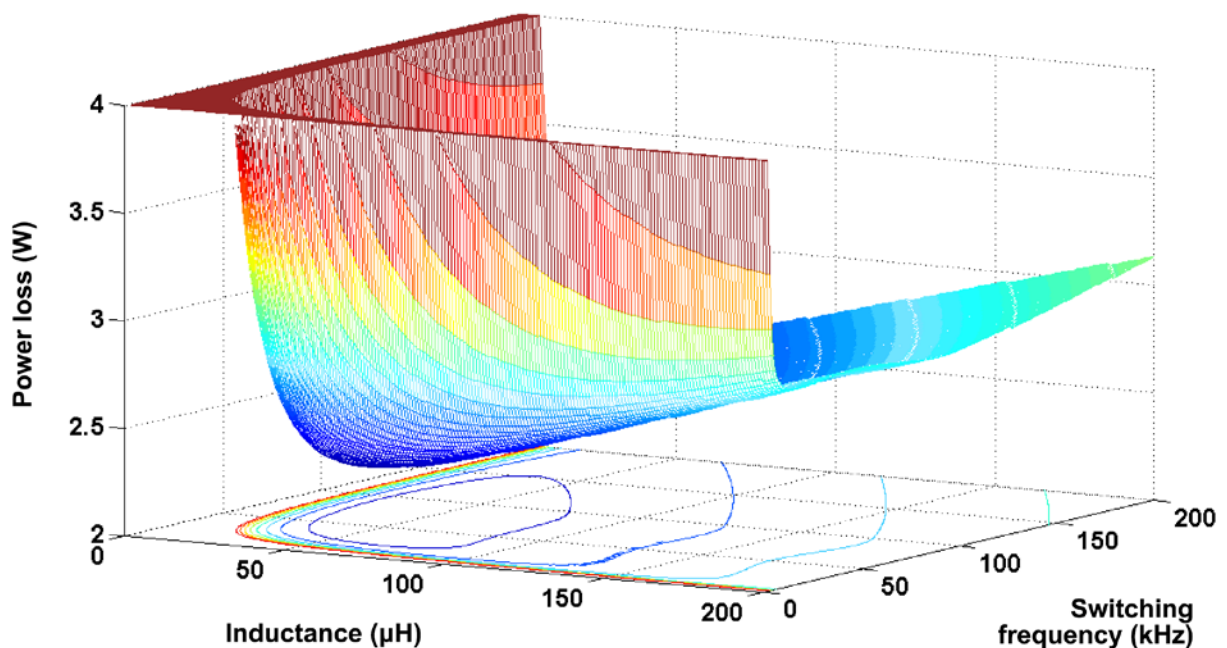


**Fig. 11.** Total power loss of the DC-DC converter for various values of switching frequency and inductance. The values above 4 W were trimmed for illustration purposes.

The simulation results presented above indicate that due to the non-linear nature of the total power loss function, the use of an efficient optimization tool such as Genetic Algorithms (GAs) is indispensable.

According to the aforementioned information that can be combined with the knowledge of the power loss behavior for all the other components, it becomes evident that a global minimum exists in every scenario. That said, the reader must keep in mind that this surface is to be linearly constrained in all cases when complying with the linear constraints of Table 7.

**Table 7.** The constraints of the circuit-level optimization process.

<i>Flags (Incident Sensing)</i>	<i>Constraints (due to component fail tolerances and load regulation specifications)</i>
1	The inductor makes the circuit get into DCM
2	MOSFET reached half of its maximum current ratings
3	Output ripple current too high
4	Output ripple voltage too high

One of these cases is studied and simulated in Fig. 12 and Fig. 13, respectively. The simulation code that produces Fig. 12 is plotting the envelope of the graph (a) in Fig. 9 but this time taking into consideration the constraints of Table 7, locating the actual operating point above which all constraints are met. The incidents that happen in every frequency value are devaluing the credibility of the respective operating points (in this example all below 31.1 kHz) are analytically presented in Fig. 13. The results show that if there were no constraints to be applied, the optimal switching frequency of the specific DC-DC converter would be set at 31.1 kHz and the simulated thermal power dissipation would be 2.45 W.

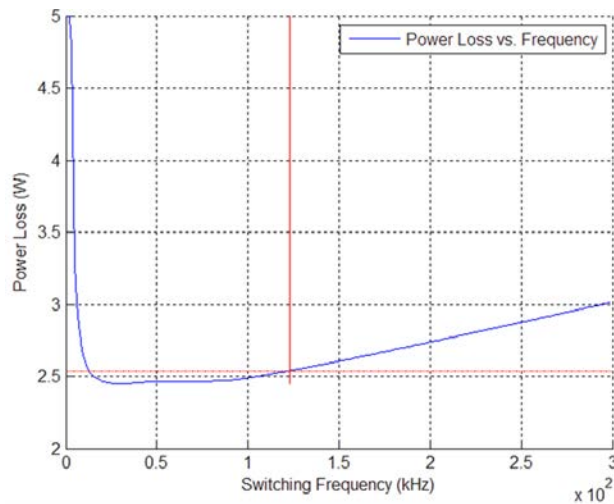


**Fig. 12.** The upper right square area that is defined by the mutual orthogonal lines holds the values that meet the constraints specifications. The lowest value of power losses in this scenario lies at the crosssection point.

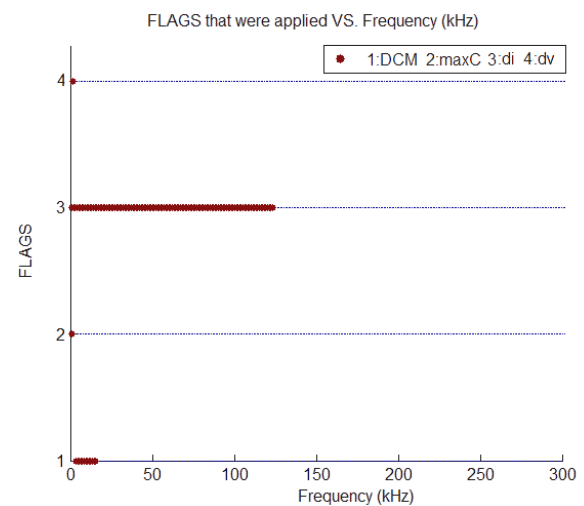


**Fig. 13.** The flags that are triggered in the chosen spectrum of switching frequencies for the chosen simulated scenario (where  $L=100\mu\text{H}$ ).

Due to the constraints though, the system must run with a switching frequency of 123.1 kHz, thus dissipating 2.539 W, which stands for a 3.6 % additional power loss. It is always the case that constraints will make the circuitry to work in a range that produces higher power loss. This was both theoretically and experimentally proven. As expected, there is always a tradeoff between component tolerances or power conditioning specifications and overall efficiency.

The previous results were immediately followed by more extended and double checked simulations which follow the general notion as before which is that in order to optimally exploit the power generation capacity of the installed PV source, the power processing interface must be designed so that the generated power is efficiently interfaced to the battery bank. This is once more achieved by applying the same optimization method for designing the circuit of the DC-DC converter, as it has already been analysed. This time the extended

objective functions are three in total and include, along with the efficiency metric (i.e. ‘Power loss at maximum output power’) and the LCOE, the ‘Total energy loss during the year’.

**Table 8.** The optimal values of the design variables.

Design Variable	Objective function		
	<i>Power loss at maximum output power</i>	<i>Total energy loss during the year</i>	<i>LCOE</i>
$MF_{Count}$	1	1	1
$L$	95 $\mu$ H	122 $\mu$ H	77 $\mu$ H
$C_{out}$	3000 $\mu$ F	3000 $\mu$ F	32 $\mu$ F
$f_s$	128.4 kHz	153.9 kHz	242.3 kHz

The resulting optimal values of the design variables for the three alternative objective functions are presented in Table 8. It is observed that a different set of optimal values is derived in each case, since, in contrast to the efficiency at nominal output power, the annual energy loss and LCOE metrics incorporate the impact of the continuously variable input power of the PV power-supplied DC-DC converter during the year. Also, the LCOE metric additionally takes into account the DC-DC converter manufacturing cost.

**Table 9.** The DC-DC converter performance for the alternative objective functions, which have been employed in the proposed optimization process.

Metric	Objective function		
	<i>Minimum power loss at maximum output power</i>	<i>Minimum total energy loss during the year</i>	<i>Minimum LCOE</i>
<i>Efficiency (%)</i>	<b>93.0 %</b>	92.3 %	92.0 %
<i>Total energy loss during the year (kWh)</i>	5.784 kWh	<b>5.670 kWh</b>	6.015 kWh
<i>LCOE (€/Wh)</i>	0.136 €/Wh	0.140 €/Wh	<b>0.119 €/Wh</b>

The DC-DC converter performance for the alternative objective functions, which have been employed in the proposed optimization process, is illustrated in Table 9. For each objective function optimized, the resulting set of optimal values of design variables (i.e. Table 8) has been applied for calculating the values of the other two objective functions and the corresponding results are also presented in Table 9.

In case that the DC-DC converter is optimized for achieving minimum power loss at nominal output power, then the resulting efficiency is higher by 0.7-1.0 % than the efficiency obtained when applying the  $E_{L,tot}$  and  $LCOE$  objective functions [given by (14) and (15), respectively]. Similarly, the minimum total energy loss is lower by 2.0-5.7 % than the annual energy loss resulting when optimizing the power loss at maximum power and  $LCOE$ , respectively. The optimal  $LCOE$  value is lower by 8.8-15.0 % than the  $LCOE$  of the DC-DC converters which have been optimized for minimum power loss (either at maximum output power, or annual power loss). The proposed GA-based optimization process was accomplished by the developed software program in about 40 minutes, with a precision of less than 1 %.

### **3.2. System-level optimization**

The proposed optimization method has been implemented by developing a simulation program under the MATLAB platform. As an example, a screenshot of the spreadsheet containing the operational data, which are provided by the designer in the proposed design optimization algorithm, is shown in Fig. 6. Each row corresponds to a different PV module type. As analyzed, the proposed optimization process is executed for each of them, in order to derive the overall optimum type of PV modules. A similar spreadsheet is input by the designer to the optimization algorithm for each device comprising the RES system under design (e.g. W/Gs, batteries etc.), according to the block diagram of Fig. 1. In order to investigate its

performance, the proposed optimization method has been applied for the optimal design of the power-supply system of a WSN node with an electric load, which consumes approximately 3 W continuously during the day. This power consumption has been derived by experimentally analyzing the corresponding requirements of the sensor and data-acquisition/wireless-transmission units employed in a WSN node, which is installed in the area of Chania in Greece. The meteorological conditions at that installation site, which were considered during the execution of the optimization process, are illustrated in Fig. 14.

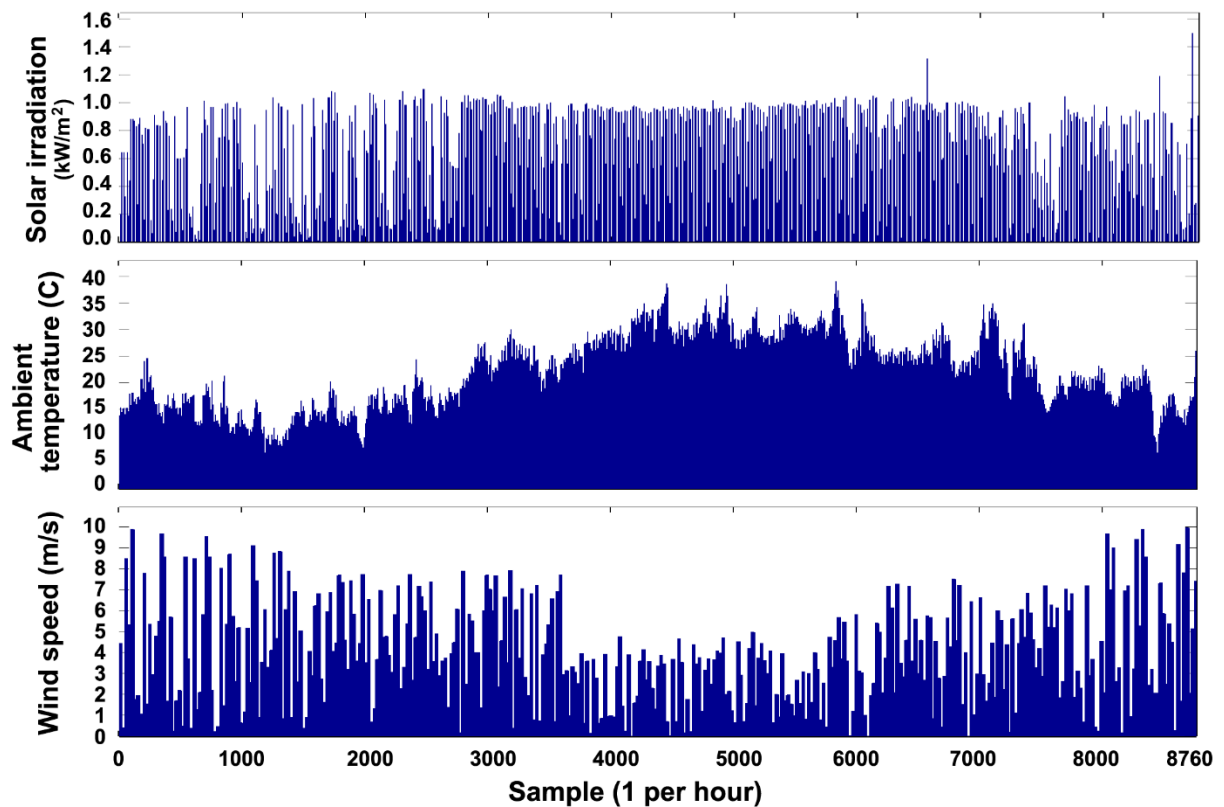


**Fig. 14.** The time-series of solar irradiation, ambient temperature and wind speed during the year, which were used in the optimization process.

The prices of the RES system devices, which are available in the local market, have been considered in this study. Thus, the operational and economic characteristics of commercially available PV modules, W/G and sealed lead-acid battery that were input in the proposed optimization process are presented in Table 10.

**Table 10.** The operational characteristics of the RES-based power-supply system units.

	<i>Solar Panel</i>	<i>Wind Generator</i>	<i>DC-DC Boost Converter</i>	<i>Battery</i>
<b><i>Rated Power per unit (W)</i></b>	<i>Rated power: 20 W (under STC)</i>	<i>Rated power: 30 W (at 10 m/sec)</i>	<i>Nominal power: 50 W</i>	<i>Capacity: 7.2 Ah</i>
<b><i>Capital cost per unit (€)</i></b>	28	108	85	9.2
<b><i>Maintenance cost per unit and per year (€)</i></b>	1.65	15	1.5	1.4

**Table 11.** The optimal values of the design variables.

<b><i>Parameter</i></b>	<b><i>Objective function</i></b>		
	<b><i>Optimized PV-based system</i></b>	<b><i>Optimized W/G-based system</i></b>	<b><i>Non-optimized PV-based system</i></b>
Rated Power (W)	40	30	60
Number of PV modules in series	1	-	1
Number of PV modules in parallel	2	-	3
Tilt angle (°)	28	-	60
Number of W/Gs	-	1	-
W/G height (m)	-	13	-
Number of batteries in papallel	4	132	4
<b>Total lifetime cost of the power-supply system (€)</b>	<b>281</b>	<b>3183</b>	<b>325</b>

The RES system lifetime has been set equal to 10 years, which corresponds to the planned lifetime of the WSN under consideration. The design optimization results indicate that for the specific installation site under consideration, the total lifetime cost of the WSN node power-supply system is minimized by using a PV source instead of a W/G. Also, the lifetime cost of the optimized PV system is lower by 13.5 % compared to the total cost of the non-optimized PV system. Thus, by applying the proposed technique, economically optimized configurations of the WSN node power-supply system are derived. The resulting optimal values of the design variables and objective function, in case that the WSN node is power

supplied by either a PV source or a W/G, respectively, are depicted in Table 11. Fig. 15 presents the time-series of the power generated by the PV and the W/G, respectively.

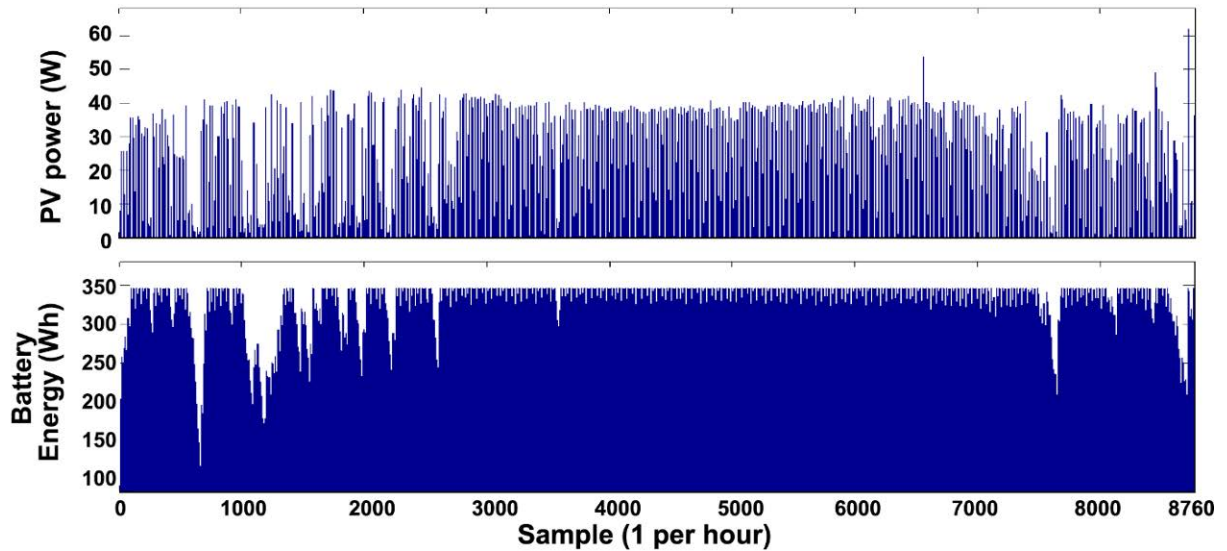


**Fig. 15.** (a) The power produced by the PV source and the energy stored in the battery bank in the simulated time-series during the year in the optimized RES-based power-supply systems.

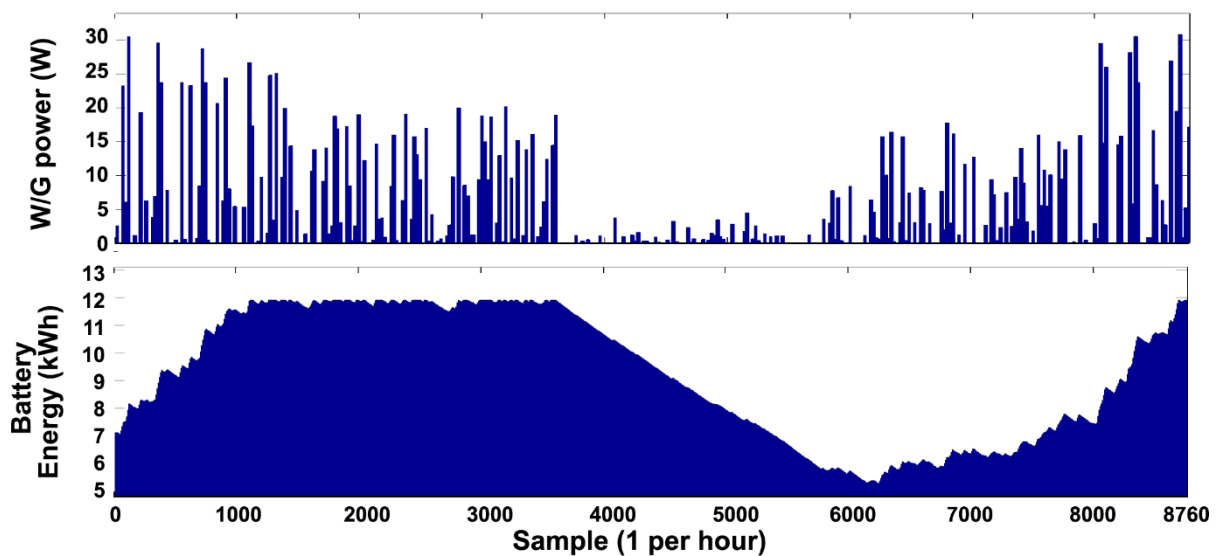
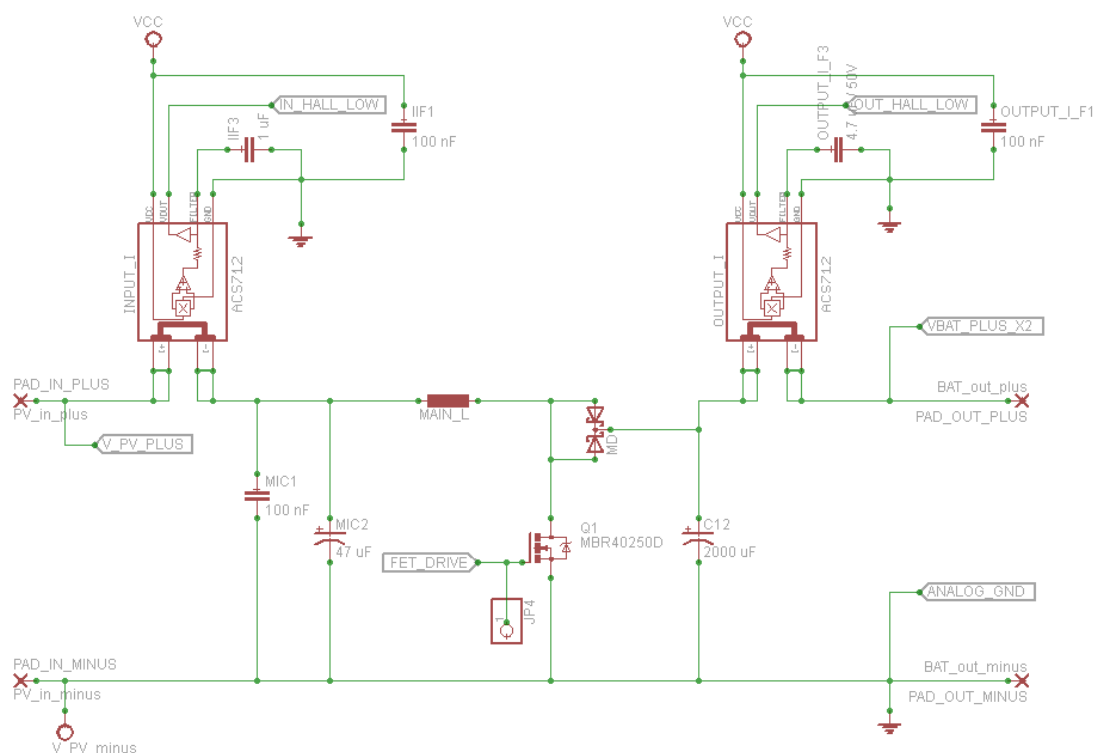


**Fig. 15.** (b) The power produced by the W/G and the energy stored in the battery bank in the simulated time-series during the year in the optimized RES-based power-supply systems.

The corresponding results in case of a non-optimized power-supply system are also presented in the same table. For both RES types considered, the optimization algorithm has properly selected the capacity of the battery bank, such that the stored energy never drops below the minimum permissible limit of 20 % of the nominal battery capacity, which was initially specified by the designer, thus fulfilling constraint (ii). The ability of GAs to derive the global optimum solution has also been verified by applying an exhaustive search process, which, however, requires a several times longer execution time in order to be accomplished. The non-optimized power-supply system comprises PV modules and has been designed as described in [57], such that the constraints (i)-(iii) (Section 2.2.3) are satisfied during its yearly operation. It is observed in Table 11 that a different set of optimal values is produced, depending on the type of the RES source, which is employed in order to build the RES-based power-supply system of the WSN node. Due to the higher cost of the W/G considered in this study and the relatively low wind-speed potential of the installation site, the total lifetime cost of the power-supply system based on PVs is 11.3 times lower, compared to that obtained when a W/G is employed.

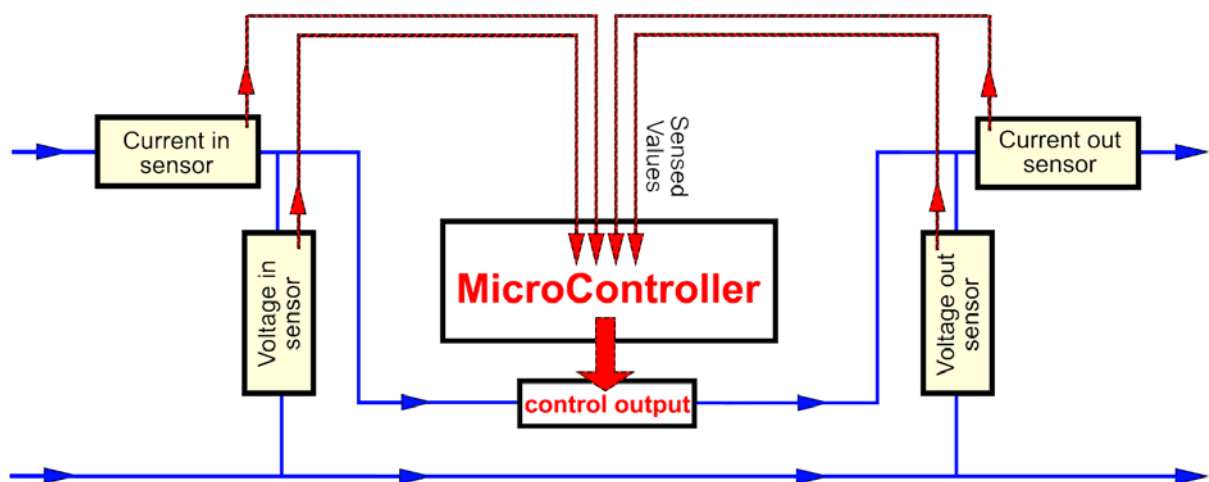
## 4. Prototype Implementation

The proposed design optimization methods have been applied for the optimal design of a WSN node, which is installed in the area of Chania (Greece). The power consumption of the electronic circuits of the WSN node is approximately 3 W. It is worth noting that the choice of components that were used at the energy generation and management system (e.g. solar panels, batteries, DC-DC converter, etc.) were realized by a systematic research on the current international market, taking into account both the operational characteristics of the components and their cost. Based on the results of the optimal design algorithms which have been presented in Table 11 for this energy production and management system with this consumption signature, the choice was to use 2 PV modules of 20 W power each in parallel and 4 closed type lead-acid batteries with a storage capacity of 7 Ah at 12 V.



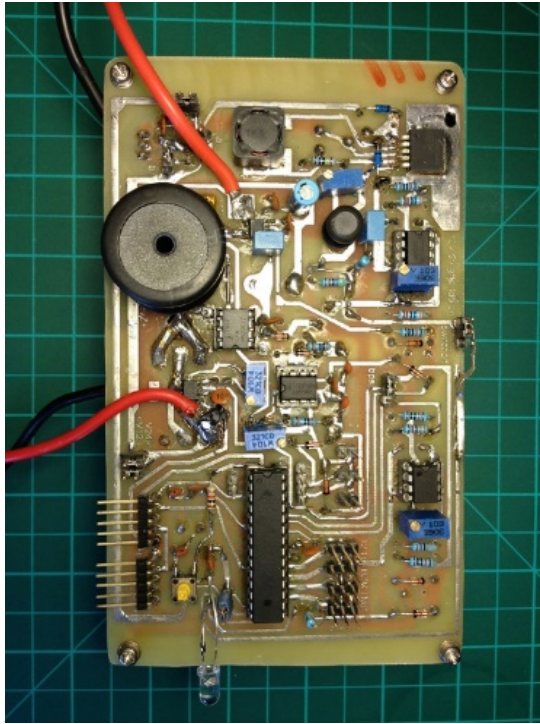
**Fig. 16.** A schematic diagram of the power sub-circuit. The two (input and output) hall-sensors, ACS712, can be seen on the top part of the image.

Fig. 16 shows the sub-circuits of the DC-DC converter, grouped according to their operating nature. The power MOSFET is driven by the microcontroller through an ICL7667 driver. Also, a 5 V voltage source was constructed for power-supplying the gate driver and signal-conditioning circuits, using the LM2596 regulator. An ATMEGA microcontroller is used to execute the MPPT and battery charging algorithms based on measurements of the input/output voltage and current of the DC-DC converter. Fig. 17 presents a block diagram of the sensors that sense the input and output voltages and currents of the converter's circuit and report back to the microcontroller who acts upon the change of the output's characteristics, closing the feedback control loop.



**Fig. 17.** A block diagram illustrating the connection of the microcontroller, the sensors and the converter's output control circuit (i.e. the MOSFET driver).

The experimental prototype PCB of a PV power-supplied Boost-type DC-DC converter, which has been optimally designed using the proposed method, is depicted in Fig. 18(a). Also, the whole setup of each node can be clearly seen in the picture taken when the containers were side-by-side at the comparison of optimized vs. non-optimized systems Fig. 18 (b)] which will be analyzed in the pages to follow.



(a)



(b)

**Fig. 18.** (a) experimental prototype of a PV-powered Boost DC-DC converter (b) workbench setup for the performance comparison of the optimized and non-optimized DC-DC converters.



**Fig. 19.** Photos of the early stage box that was hosting the converter, the batteries and the load.

The containers where the PCB of the Boost-type DC-DC converter and accompanying control circuits were installed in were carefully chosen to be used for carrying and hosting all the necessary experiment equipment including the DC-DC converter PCB and the batteries. The shape and type of the box, which meets the IP65 standard, is presented in Fig. 19.

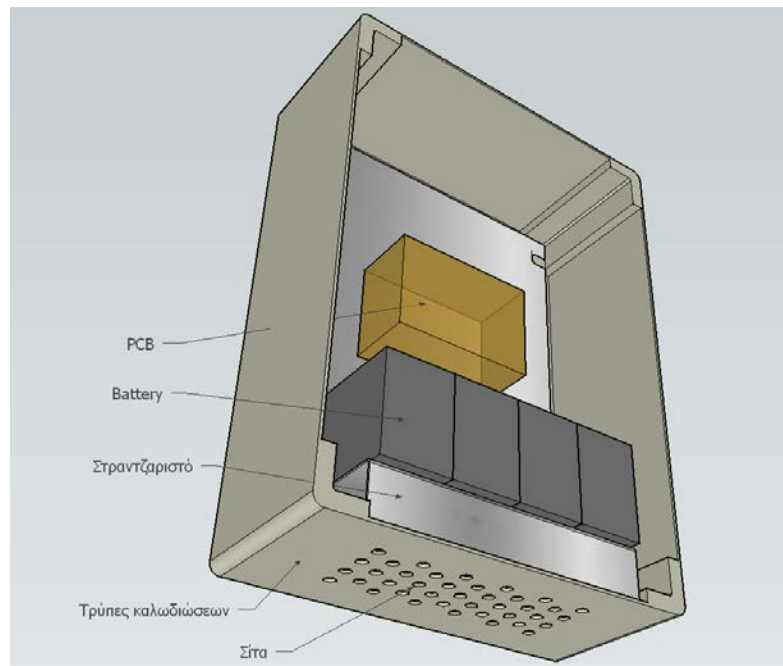


**Fig. 20.** Auxiliary 3D design for the configuration and installation modelling.

As shown in the 3D drawing of Fig. 20, which was implemented during the earlier design selection process of the mounting platform to be used to carry and protect the electronic components, there is some perforation at play. This perforation is done primarily for opening a passage for the wiring and secondly for creating a passive airflow to cool the materials within. The drilled holes for the wiring passage are done on the grounds that they will be insulated in the future as long as the conditions require it. The current versions of the box do not use the perforated shape as depicted but instead only a big rectangular hole is used and a ventilation strainer gets installed in the same space. Similarly a second strainer is fitted to a corresponding point on the top of the door of the box to ensure proper passive ventilation.



**Fig. 21.** The interior of the IP65 box with all electronic systems installed and in operation.

Fig. 21 illustrates the strainer on the door of the box as well as the layout of the PCBs at the back of the box. The batteries are firmly mounted on the bent metal frame with a thickness of 1.5 mm, as presented in the 3D design. The batteries and the bent iron frame under them is stuck to each other, as well as with the box, by using double sided tape. The converter PCB has been placed in the center of the back of the box, whereas the load was placed on top of it. Although at the final stages the load of the WSN node (i.e. a digital system board) was placed in smaller stand-alone boxes, at the early stages these boards were placed inside the big boxes that also included the converter PCB and the batteries. This was done for taking advantage of the data logging capabilities of the digital system board (i.e. WSN node load) for monitoring the operation of the proposed power-supply system which was constructed.

The optimal slope of the PV modules to be used in each region is the one calculated by the genetic algorithms and cross-checked by the MATLAB's simulations, as analyzed in Section 3.2. The preliminary tests were performed on an experimental workplace in order to collect the first data and make the suitable amendments and/or any final improvements (Fig. 22).



**Fig. 22.** Two of the prepared stand-alone systems as they were placed during the preliminary operation tests.

Those tests revealed useful conclusions related to the behavior of the power production and management system of the wireless nodes (in conditions similar to those prevailing in the water tank area). The temperatures developed inside the container were a little more than 40 degrees Celsius (in the arrangement shown in the respective figure). The front side of the PV panels developed a temperature close to 60 degrees Celsius. The positioning of the sieve at the bottom of the cans (rather than on top) lowered the temperature by 3 degrees Celsius. It is estimated that the temperature drop will be increased when the boxes get positioned at a sufficient height that will allow the air to enter into the container (from the strainer located at their base) and freely flow inside it. The PV panels shown in Fig. 22 were selected to meet the

appropriate operating specifications and hold the exact characteristics as they are defined by the results of the system level optimal design algorithm which was presented in Section 3.2.

Thereafter, the spreadsheet shown in Fig. 23 was created to assist with the calculation of the cable cross section that is required to be used for the interconnection of the PV panels with the DC-DC converter according to the established specifications (i.e. the installation length, the maximum input current, a typical input voltage, the temperature coefficient and the power losses tolerance).

International standard wire sizes (IEC 60228)					Thermal coefficient
0.5 mm <sup>2</sup>	0.75 mm <sup>2</sup>	1 mm <sup>2</sup>	1.5 mm <sup>2</sup>	2.5 mm <sup>2</sup>	
6 mm <sup>2</sup>	10 mm <sup>2</sup>	16 mm <sup>2</sup>	25 mm <sup>2</sup>	35 mm <sup>2</sup>	1.118
70 mm <sup>2</sup>	95 mm <sup>2</sup>	120 mm <sup>2</sup>	150 mm <sup>2</sup>	185 mm <sup>2</sup>	
300 mm <sup>2</sup>	400 mm <sup>2</sup>	500 mm <sup>2</sup>	630 mm <sup>2</sup>	800 mm <sup>2</sup>	
Voltage (V) < [slider] >					6
Current (A) < [slider] >					6.5
Length (m) < [slider] >					12
Conductor size (mm <sup>2</sup> )	Conductor resistance (Ω/1000m)	Voltage drop (mV)	Power in (w)	Power loss (mw)	% loss
1.5	11.900	2,075.46	39.00	13,490.46	34.59
2.5	7.140	1,245.27	39.00	8,094.28	20.75
4.0	4.470	779.60	39.00	5,067.42	12.99
6.0	2.970	517.99	39.00	3,366.95	8.63
10.00	1.77	308.70	39.00	2,006.56	5.15
16.00	1.13	197.08	39.00	1,281.03	3.28
25.00	0.712	124.18	39.00	807.16	2.07
35.00	0.514	89.65	39.00	582.70	1.49
50.00	0.38	66.10	39.00	429.65	1.10
70.00	0.262	45.69	39.00	297.02	0.76
95.00	0.189	32.96	39.00	214.26	0.55
120.00	0.150	26.16	39.00	170.05	0.44
150.00	0.122	21.28	39.00	138.31	0.35

**Fig. 23.** Spreadsheet with macros that automate the calculation of the cabling power losses.

As an example, for an installation of the PV modules at a distance of 20 m away from the DC-DC converter, also considering the total weight and cost of the conductor, a cable 4x10 (E1VV-R 4G10 from Nexans) should be used, which generally presents power losses which are less than 1 % and can operate under the strong radiation conditions presenting power losses less than 3 %. The final version of the experimental prototype system which was developed is depicted in Fig. 24.



**Fig. 24.** The experimental prototype of the WSN node power-supply system, which has been designed according to the proposed optimization technique.

#### **4.1. Development of the energy management unit**

The power MOSFET of the DC-DC converter is controlled by a microcontroller-based unit, based on the decisions derived by executing a Maximum Power Point Tracking (MPPT) algorithm for maximizing the energy produced by the PV or W/G input source, as well as a battery charging algorithm for regulating the battery charging process.

There are several algorithms of MPPT control described in modern literature, some of which are specifically designed to be used in the field of PV control. According to Patrick L. Chapman and Trishan Esum in [53] as well as Roberto Faranda and Sonia Leva in [54] there are over 19 different well-known MPPT control methods and most of them lay on hill-climbing techniques. The criteria of selection lay upon the performance in relation to implementation effort, the cost of design and production and in some cases upon the requirement of reprogramming or adding regulatory adjustments. One of the most common MPPT algorithms favored for its ease of use and low computational cost is 'Perturb and Observe' (P&O).

As the name suggests this algorithm works in two stages. First it disturbs the controlled quantity in a known manner and then it evaluates the effect of this disturbance. The disruption can be based on small periodic variations of the duty cycle. A frequent sampling and a subsequent comparison of the input power values before and after the disturbance lead to a conclusion whether the change eventually contributed to the increase or reduction of the generated power. If the selected direction of the disturbance caused an increase of generated power further adjustments in that direction are tried until generated power starts to drop again. The DC-DC converter was designed to be able to operate at the maximum power point (Maximum Power Point or MPP) at all times, regardless of the RES used. To achieve this target, the Perturbation & Observation (P&O) algorithm was used since it can apply in both cases (whether a PV array or a W/G is chosen). The MPPT flowchart, which shows the decisions that the P&O algorithm performs, is shown in Fig. 25.

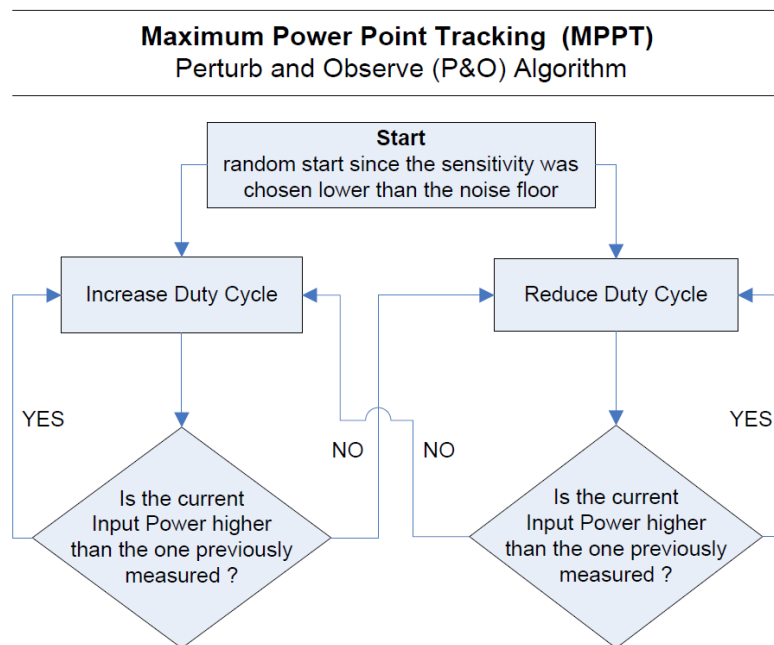


**Fig. 25.** Flowchart of the Perturbation & Observation algorithm used in the real-time MPPT process.

**Adaptive -to the battery charging requirements- trickle-charge algorithm**  
Based in the operating point of a MPPT mechanism control

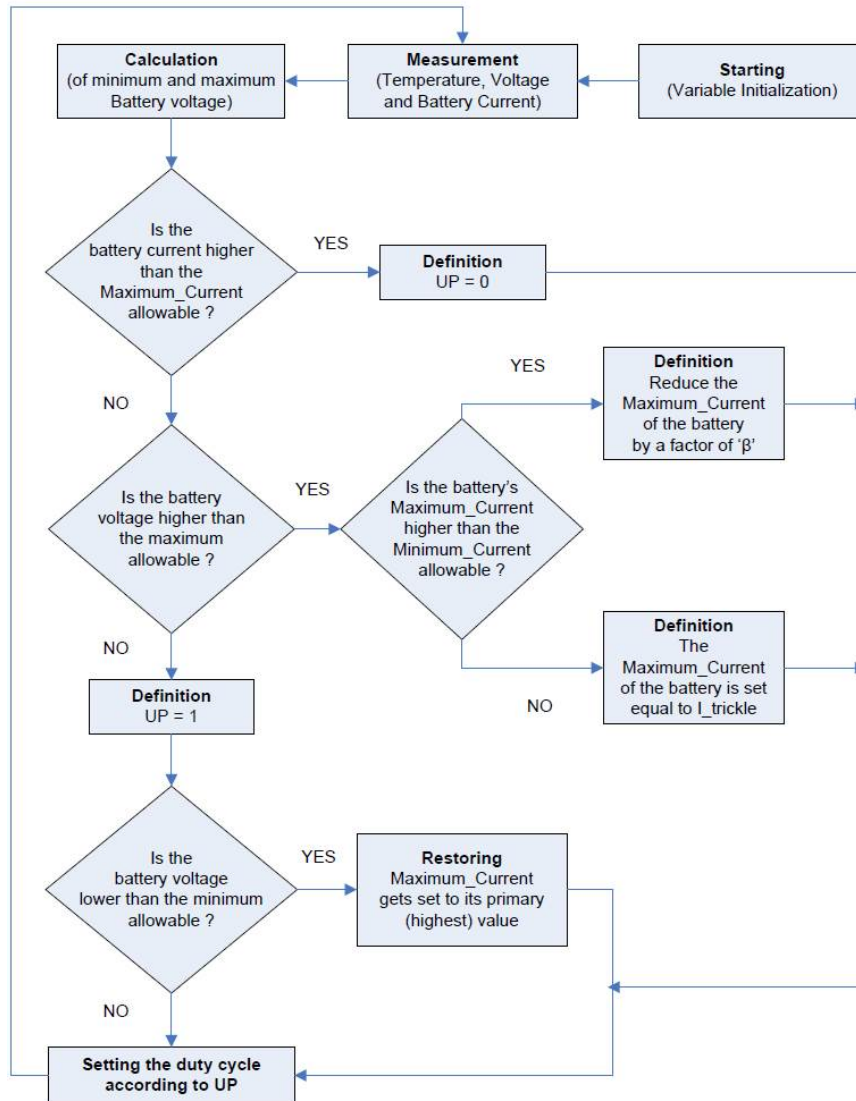


**Fig. 26.** Flowchart of the battery charging control algorithm that presents the battery charging process.

It was decided that the MPPT algorithm will not be operating continuously but rather be controlled at a certain pace by using a trickle charge mode that can keep up with the major aim which is not to overload the batteries and expand their life span. The trickle charge mode is designed to adjust the charging current amplitude and rate depending on the battery's charge state and this is done by indirectly controlling the MPPT mode through the alteration of its duty cycle goal level and subsequently its operating point setting [34]. This special

controlling of the state of the MPPT is feasible since the nature of the MPPT algorithm and the way it is controlled do allow this auxiliary operation that in turn assists in the proper adjustment of the battery charging current. Setting this value properly is necessary in order to achieve the best reliability possible while keeping up with the optimal use of the generated energy. Fig. 34 shows the flowchart of the battery charging control algorithm.

The next step was to confirm the proper operation of the automated duty cycle level setting algorithm, which ensures that the battery voltage will always be at a level lower than the maximum allowable according to the user's adjustment.

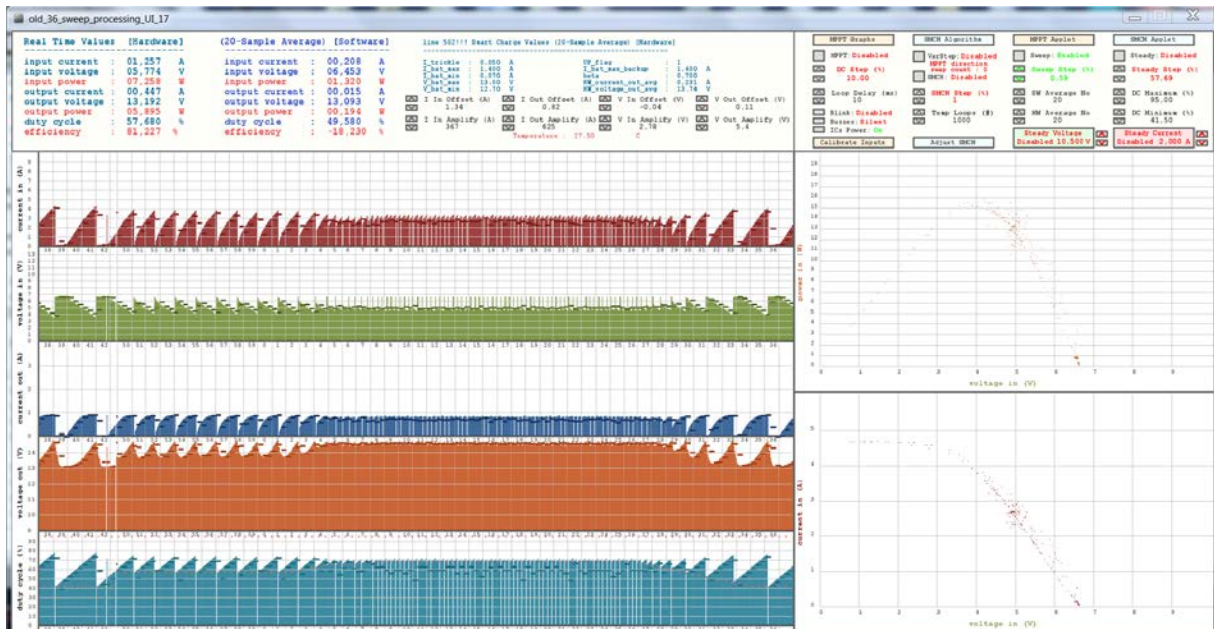


**Fig. 27.** Confirmation of the expected behavior of the voltage regulation control sub-system that keeps the battery's voltage amplitude below the maximum allowable limit.

As it can be shown by looking closely at the current and voltage waveforms in the diagram of Fig. 27 (from top to bottom: input current, input voltage, output current, output voltage, duty cycle) the DC-DC converter successfully keeps the output voltage level under the 14.7 V, exactly as it is specified by the rules of the corresponding algorithm, regardless of the rate that the circumstances for an over-voltage event appear. Similar to this is the trickle-

charge algorithm function which lowers the maximum allowable charging-current every time a set of rules decide to do so, in order to keep the battery's state of charge in the optimum level and expand its life-span by putting less electrochemical stress on its crystals.

Also, one of the important steps of the development process that could reveal a lot about the sensors of the DC-DC converter circuit and the specifications of the PVs at hand was the characterization of the solar panels (i.e. recording the characteristic curves of the PV panels).

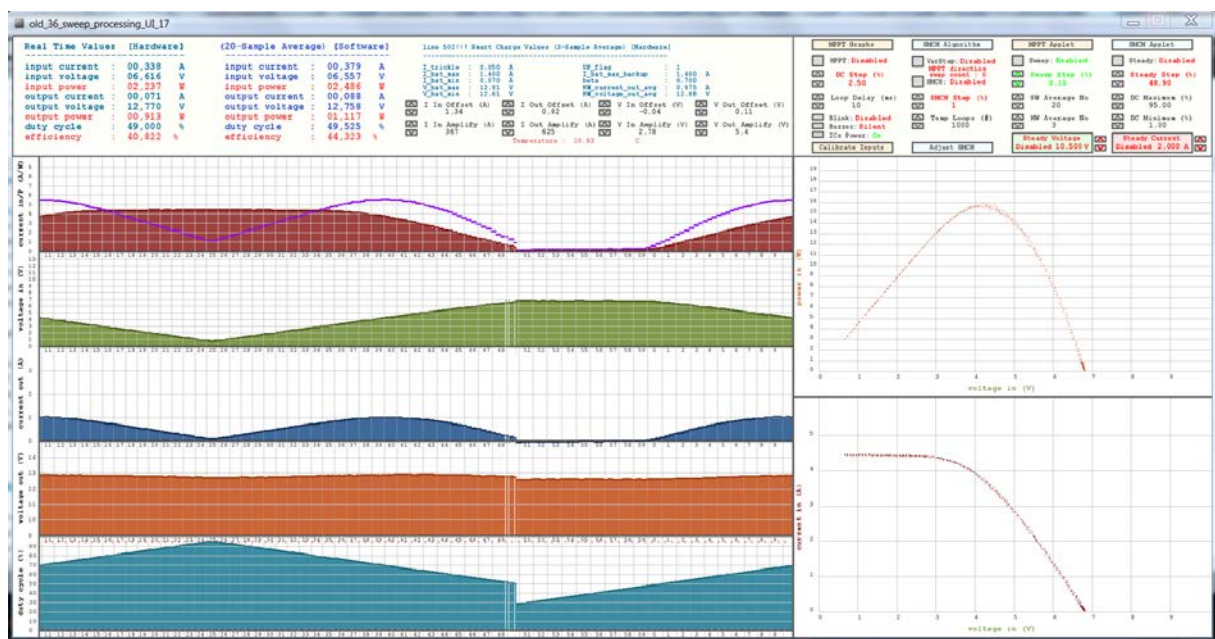


**Fig. 28.** Characteristic P-V και I-V curves of a single 20 W PV panel.

Special code was developed to make a proper scanning and create the power-voltage (P-V) and current-voltage (I-V) curves which are indicative of the proper functioning the PV cells of every panel. The curves that were formed by sweeping the duty cycle values extracted the expected results proving that both the PCB sensors and the manufacturing specifications were exact and finely tuned.

Towards the same goal what followed was the cross-check of some typical values such as the short circuit current, the open circuit voltage and the maximum possible power output.

These were also measured to be exactly on the spot like it was anticipated before comparing them with those provided by the manufacturer. The cross-check included the testing of 40 PV panels. As far as it concerns the curves, judging by the randomized checks run on eight panels, it was found that all of them were operating according to specifications set by the manufacturer. Fig. 28 shows a screenshot taken while conducting one of these tests. Having outlined the operating curve of the PV panels, the next step was to start the Maximum Power Point Tracking (MPPT) algorithm before significantly changing the environmental conditions so as to point out the area around which the operating point is settling.

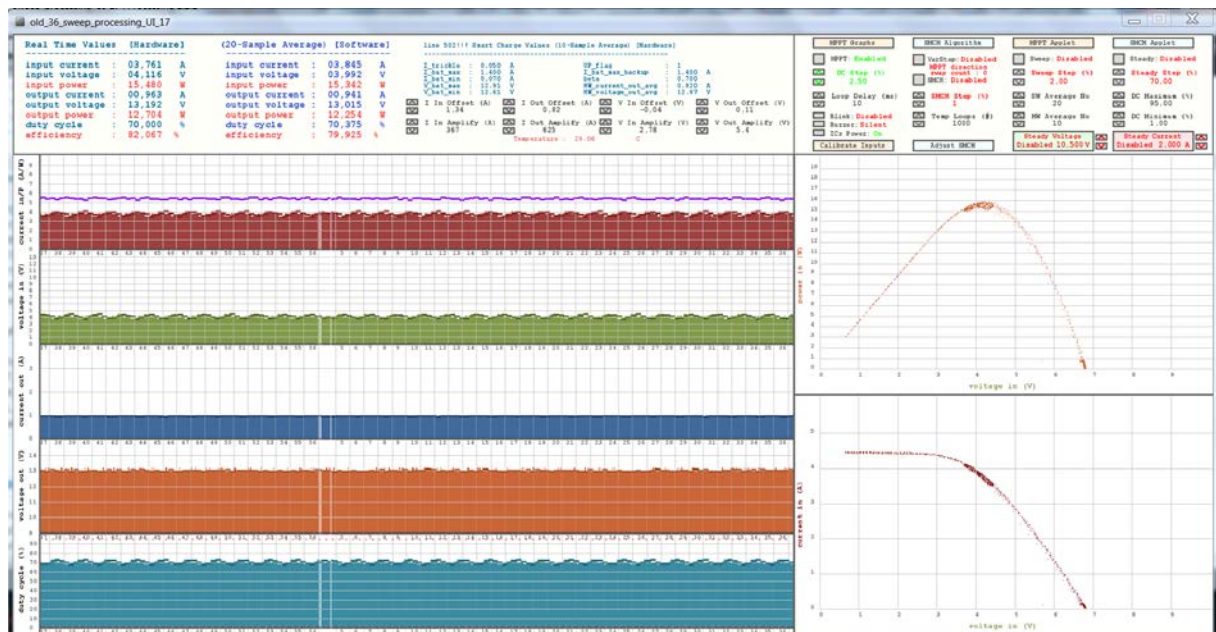


**Fig. 29.** Confirmation of the proper functioning of the MPPT process.

As it is shown from the screenshot of Fig. 29, the additional cloud of sample points is located around the MPP confirming the proper operation of the algorithm. In this image the duty cycle was set to vary in perturbation steps of 2.5 % and the maximum power generated by the PV panel was found to be about 16 W. From the various tests that were conducted it was found that the power produced by the panels exceeded the nominal value, i.e. 20 W, several times during the days of July (year 2014). This is normal and quite expected for the climate of the

installation area (Chania, Greece), since solar radiation conditions sometimes prevail a solar intensity of more than 1000 Watts per square meter. To examine the adaptability of both the hardware and the software implemented around the converter into different topologies and conditions, a new behavior of the DC power source was introduced. The choice made was to test the design where such modifications could be applied, by connecting two PV panels in series, open-circuit voltages that reach 14 V, which practically translates into feasible MPP voltages slightly below the 12 V mark. The delineation of the new P-V curve and the functional testing of the MPPT algorithm were recorded in two different times for two different sunlight's intensities. As it can be seen in Fig. 30, both the PCB and the power management algorithm behaved exactly as expected.

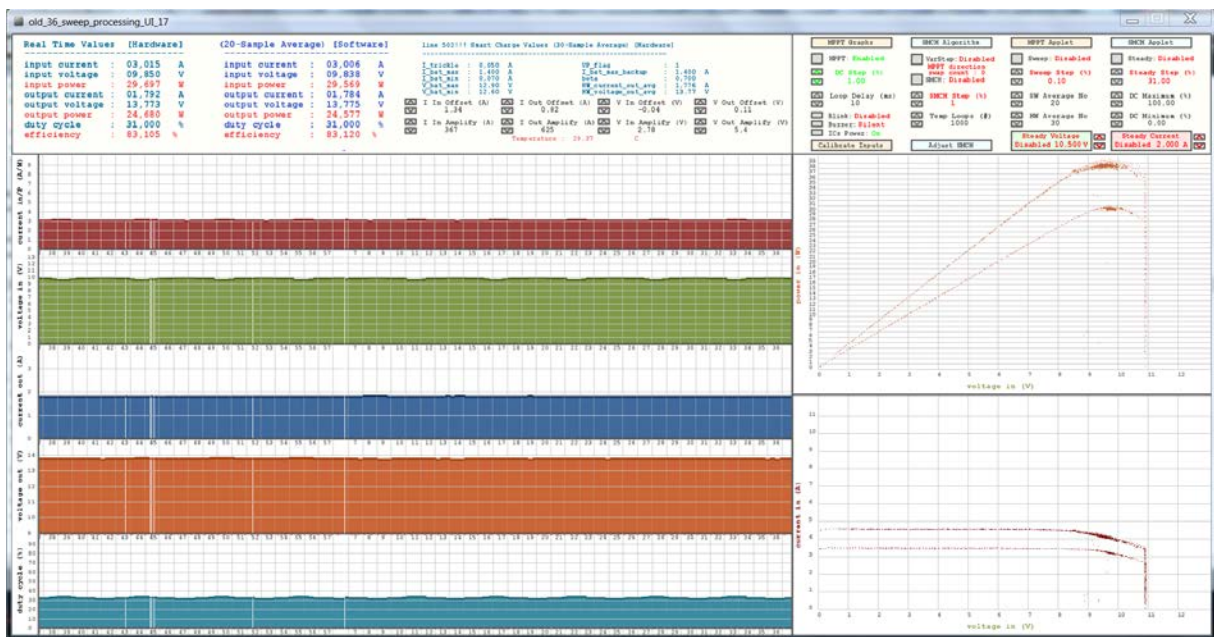


**Fig. 30.** Confirmation of proper functioning of the MPPT process for different operating points.

Subsequently, the two PV modules were connected in parallel, which is exactly as it was prescribed for the needs of the wireless nodes. Once again, the behavior of the algorithm was sampled in two phases, firstly by sweeping the duty cycle and secondly by switching on the

MPPT algorithm, thus keeping the setting point around a preferable duty cycle value, the one corresponding to the maximum of the generated power possible at that time. The test was repeated for 3 different values of duty cycle stepping. Fig. 31 illustrates the collected results of this test. In order to make the phenomenon under study become more noticeable, the tests were made during the afternoon where the sun is quite set and the radiation is relatively reduced producing P-V and I-V characteristics of greater curvature thus challenging the MPPT / P&O algorithms to converge to the optimum operating point.

Thereby, although it is acknowledgeable that the changes in the weather conditions may produce some additional declinations in the measured quantities during the test, the mixed results can still reveal a lot about the performance of the DC-DC converter implementation.

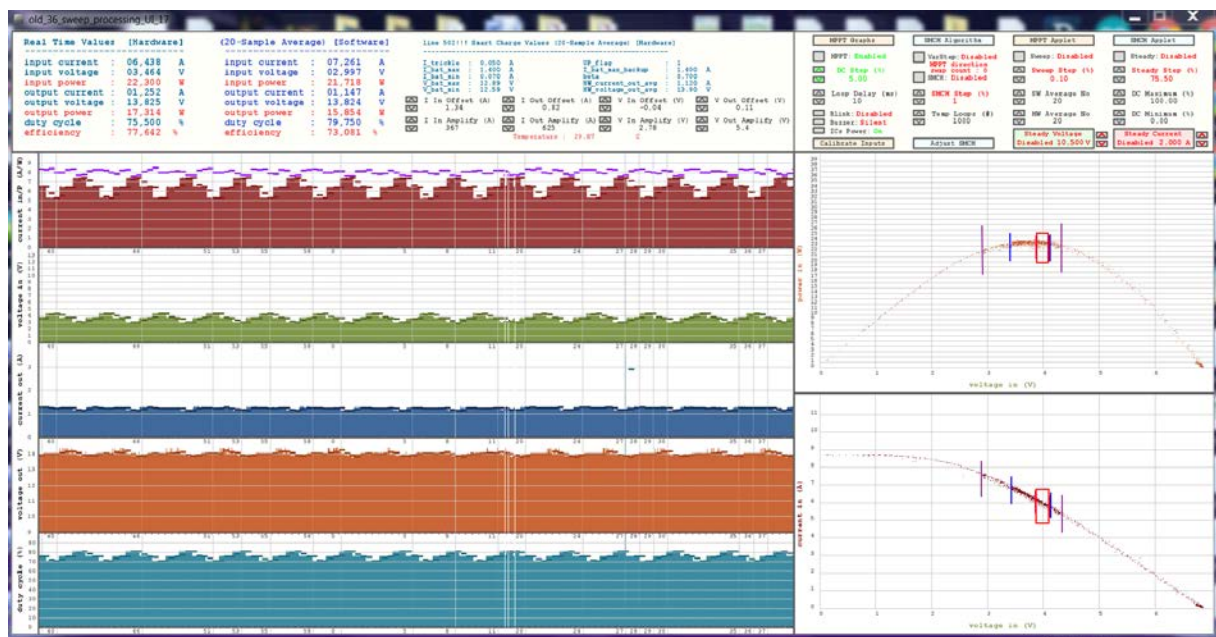


**Fig. 31.** MPPT algorithm performance check parametrically to different values of duty cycle perturbation.

The changes in the duty cycle stepping under the aforementioned conditions resulted into the following voltage and current fluctuation ranges:

- duty cycle perturbation step = 5% is : 1.40 V, 2.0A (vertical purple lines)

- duty cycle perturbation step = 2.5% is : 0.75 V, 1.3A (blue lines)
- duty cycle perturbation step = 1% is : 0.25 V, 0.5A (red box)

whereas the deviation of the MPP is less than 8.3 %, 4.2 % and 2 %, respectively. The same data regarding the MPPT performance in relation to the duty cycle stepping are collected and grouped in the form of a matrix in Table 12.

**Table 12.** MPPT performance in relation to duty cycle stepping

Case	Duty Cycle Step values and variations from MPP			
	Duty Cycle Step	Voltage Range p-p	Current Range p-p	Power Deviation
A	5.0 %	1.40 V	2.0 A	8.3 %
B	2.5 %	0.75 V	1.3 A	4.2 %
C	1.0 %	0.25 V	0.5 A	2.0 %

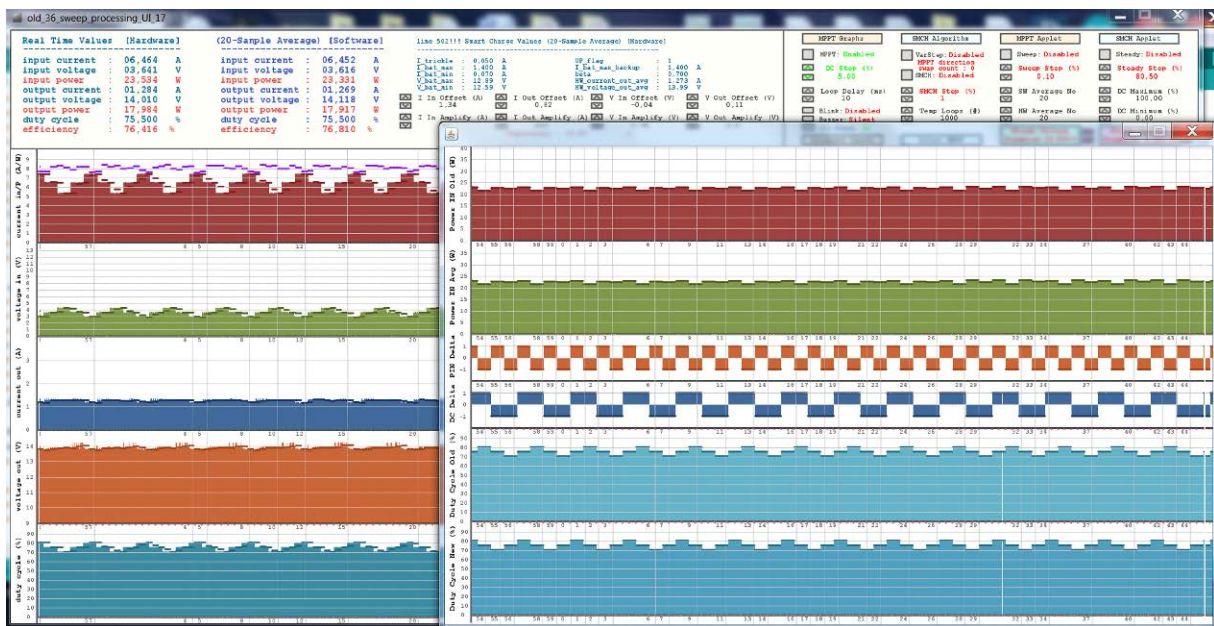


**Fig. 32.** Applet screenshot that monitors the metrics which demonstrate that the MPPT follows the right decision steps.

Lastly, the proper functioning of the algorithm (without skipping steps) was confirmed by using an appropriate applet that displays all decision metrics in real time. Specifically, Fig. 32

shows the preceding and succeeding values of the input power (the first two graphs), the preceding and succeeding values of the duty cycle (the last two graphs) and their variations (in the two middle graphs).

As shown before, both plots in Fig. 33 have been produced by real-time captured data through the use of the interface that was developed for the customization and debugging of the DC-DC converter circuit.

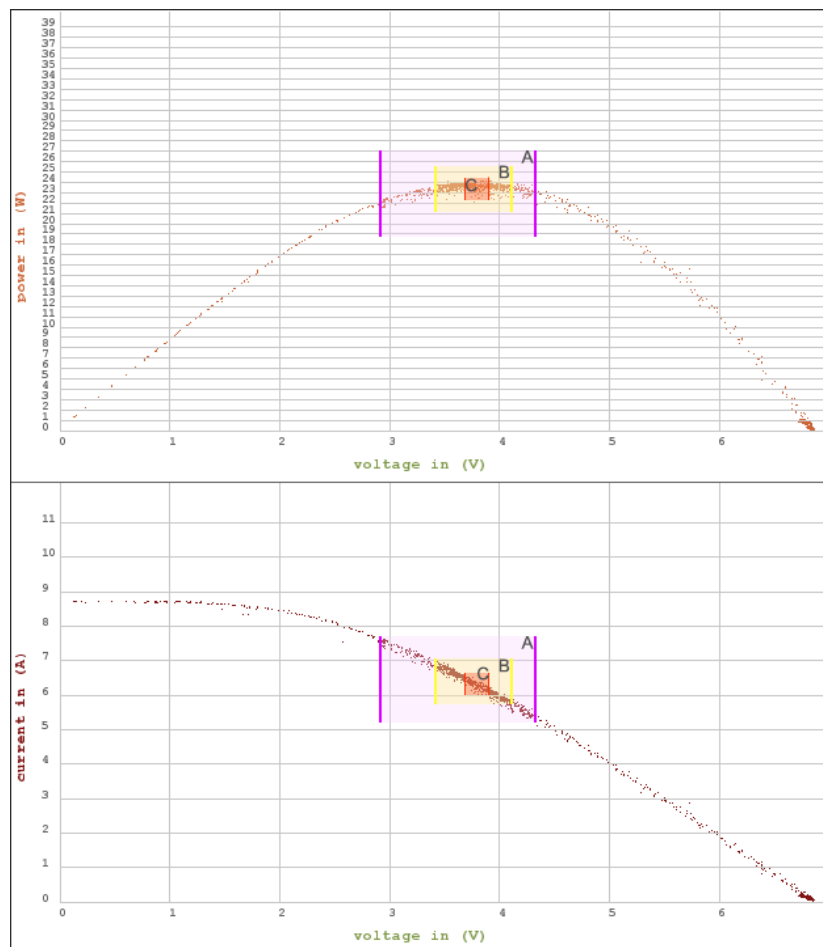


**Fig. 33.** Characteristic Curves (P-V and I-V) of the solar panels attached on the input line of the DC-DC converter. The MPPT algorithm spots the correct operating point in all cases. Its deviation is due to the duty cycle stepping.

A screenshot of this interface is also shown but in less detail in Fig. 31. The characteristic curves were sketched while the system was running on 'Sweep' mode, changing the duty

cycle of the PWM of the MOSFET driver by small increments (up to 99.5 %) and then by small decrements (down to 0.5 %) looping back and forth. While the duty cycle's values were ranging in that spectrum, the microcontroller was sampling the input current and voltage shaping the curves as depicted in the respective figures. After 5 minutes the mode was changed to 'MPPT' and the microcontroller started running the P&O algorithm that settles around the operating point that produces the maximum power possible. This mode produced the accumulation of the dots in a close neighborhood around the center of each graph, close to a very specific point that under steady weather conditions is being kept constant.

What followed after the MPPT P&O tests was the comparison of the behavior of two circuits, differentiated only by the main inductor's characteristics. More specifically, the inductance and the ohmic resistance of one of the PCB's main inductor was reduced by a factor of 2 (i.e. in half) by soldering two inductors of the same kind in parallel (since there were many available inductors of this type). This translates into a different inductance and ohmic resistance for the inductor while all the other design features (and component values of course) remain unchanged. Many more experiments were conducted, always altering the inductance component. From the experiments it was found that this replacements caused a change in the overall power losses of the converter, which is exactly what was expected to happen in theory too. These experiments contributed to the characterization of the magnetic flux saturation curving of the coils at hand. The curves were formed in relevance to the switching frequency and parameterized by the value of the inductor inductance. The simple principle that proved to be very helpful was the known fact that after the replacement, any declination from the optimally calculated value should result in an increment of the measured power losses of the converter given, of course, that the ohmic resistance of the inductor is also kept constant or changing in an expected and precisely calculated manner.

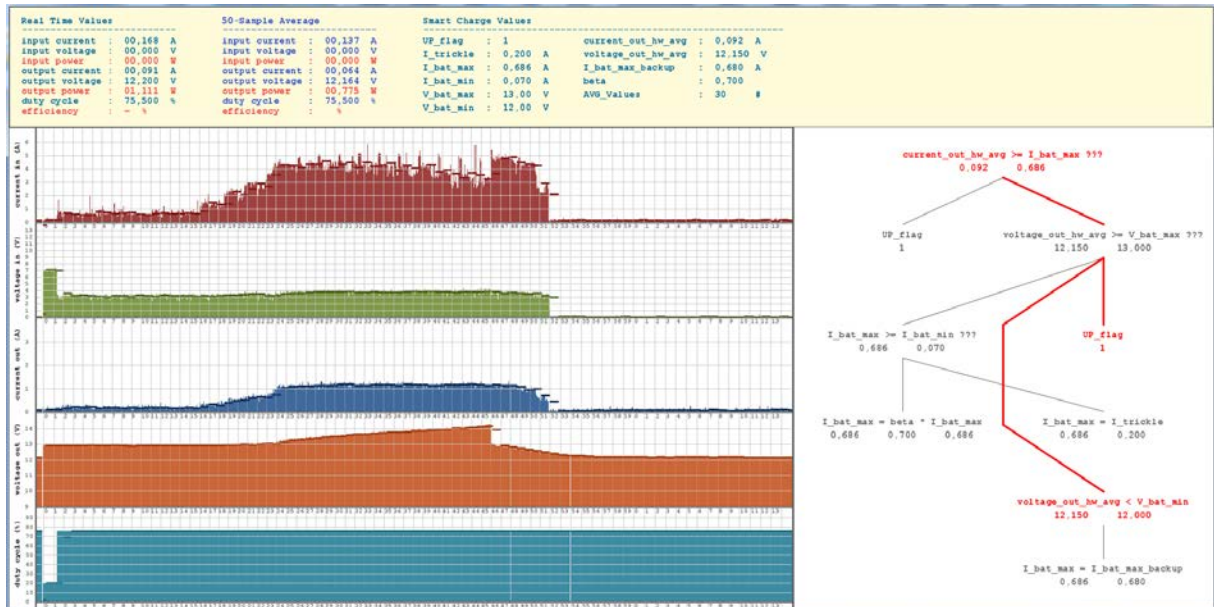


**Fig. 34.** A stripped version of the user interface. The flowchart on the right gets highlighted according to the steps that the trickle-charge algorithm follows, while it is regulating the charging process of the battery.

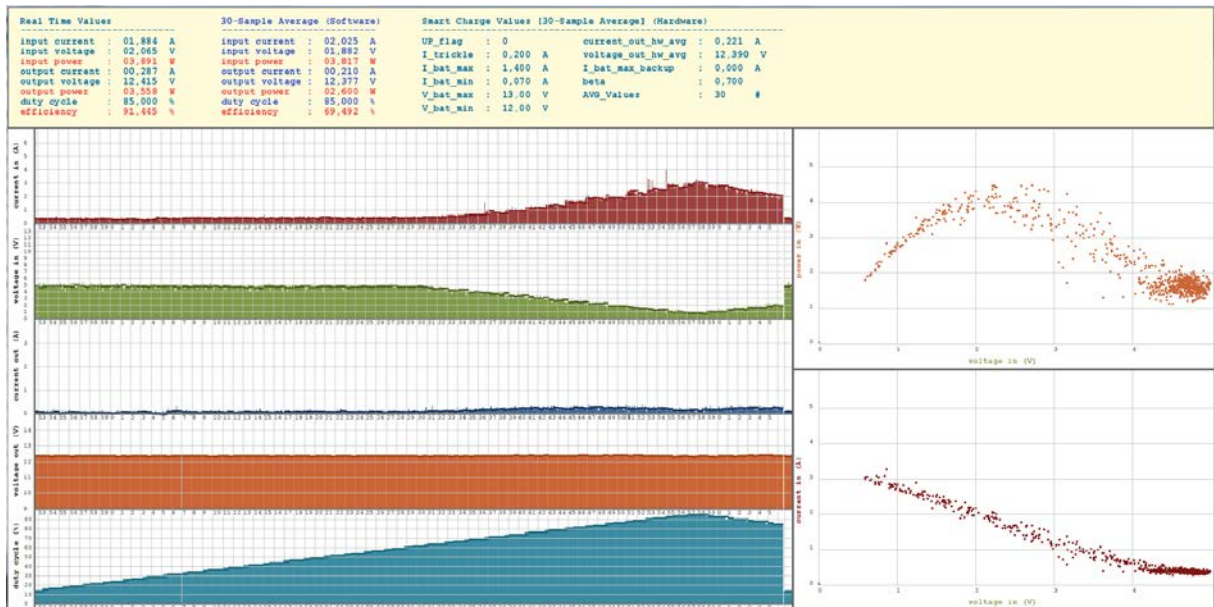


**Fig. 35.** Screenshot of the interface used for the circuit calibration and the debugging during the experimentation process. Here what is depicted is the power control interface: upper right is the P-V and lower right is the I-V characteristic of the PV panels.

This is how the practical measurement helped the experimental values to come closer to the simulated ones. This characterization process is considered to be very important since it affects the correct calculation of the outcome at the objective function evaluation phase of the sizing algorithms. Fig. 34 and Fig. 35 show instances of the interface which was implemented in order to control a number of circuit parameters that can easily examine the proper operation of the circuit and the algorithms executed by the microprocessor. The top of the screen gathers all the instantaneous values of the measured quantities (such as input current, input voltage, output current, output voltage and duty cycle) while the bottom of the screen sweeps the screen horizontally (from left to right as an oscilloscope) producing various time series for the same aforementioned quantities, displaying how these vary in time or to compare them and reason about the circuit's behavior according to the each scenario differences / needs. For example, if the scenario requires that the amplitude of noise needs to be reduced (which may stand for the appropriate choice of the number of samples -to produce the average value- and the stepping of the MPPT duty cycle) then the sampling is more frequent. If what interests the most is an overview of the time series that will reflect the proper operation of the trickle-charging algorithm, then the sampling needs to be rarer.

Immediately after the first laboratory tests of the DC-DC converter board, conducted both in realistic and in extreme conditions, it was examined whether the operation can be regarded as stable and to what extent does it meet the specifications as defined for the prototype. Since the results came out very satisfactory, new, more stringent targets were introduced related to:

1. the power consumption of the converter,
2. the value of the measured noise (of the current and voltage both in input and output),
3. the electronic noise variance range shown at the output of the converter,
4. the reduction of the microcontroller's working cycles per time unit in order to improve the sampling performance and communication with all electronic sub-systems and the load's ICs,

5. the ability to change the calibration's parameters in real time,
6. the ability to change the parameters that define the functionality of the converter and the behavior of the algorithms in real time and
7. the removal or replacement of the parts considered to be significantly reducing the final cost of the board without affecting the functionality of the circuit.

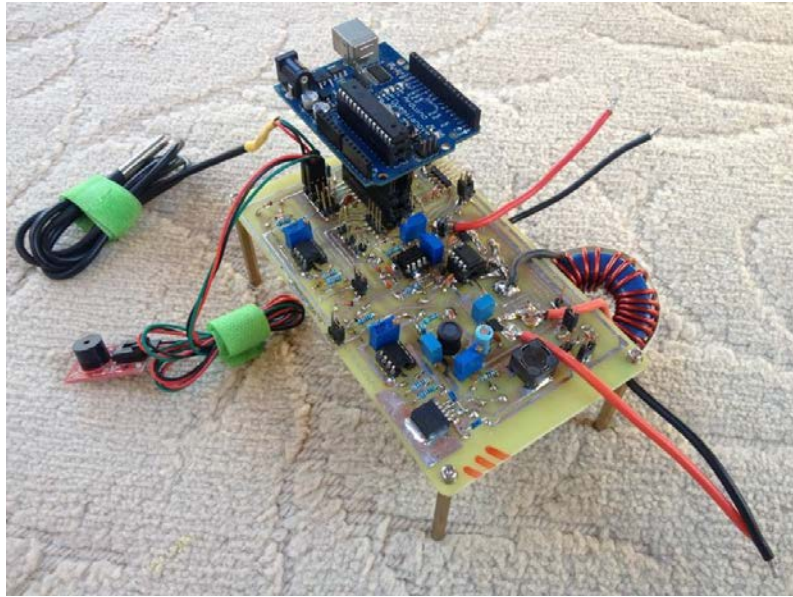


**Fig. 36.** The top side of the DC-DC converter PCB.

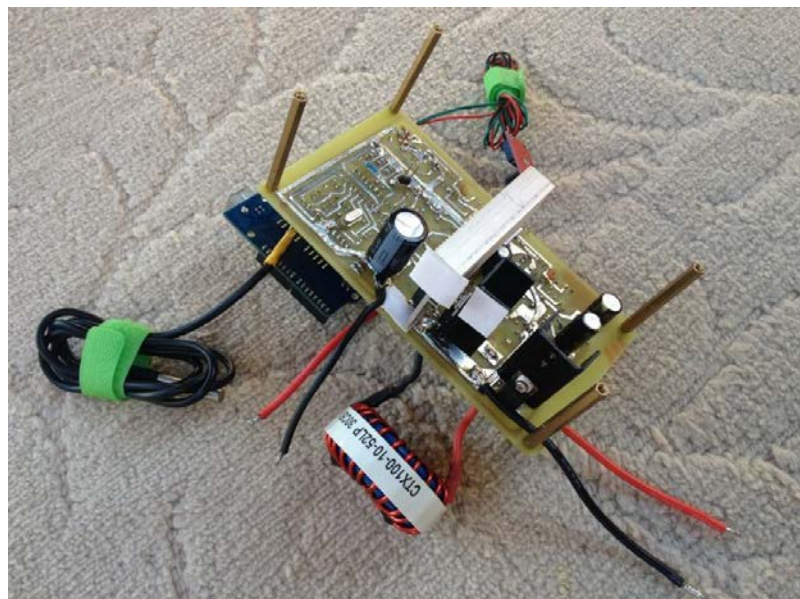


**Fig. 37.** The bottom side of the DC-DC converter PCB.

Fig. 36 and Fig. 37 present the top and bottom face of the DC-DC converter PCB. What is apparent is the various headers (signal and power terminals) that were installed to ensure the fast and convenient importing and exporting of modular sensors and actuators during the experiments (such as 'temp' and 'buzzer'). The illustrated PCB has been tested, in the operating power of 100 W (250 % greater than the corresponding maximum level possible during a typical operation on the wireless nodes) for 5 minutes and at the power of 80 W (200 % greater than the corresponding maximum level possible during a typical operation) for 60 minutes, without experiencing any problems or faults whatsoever.

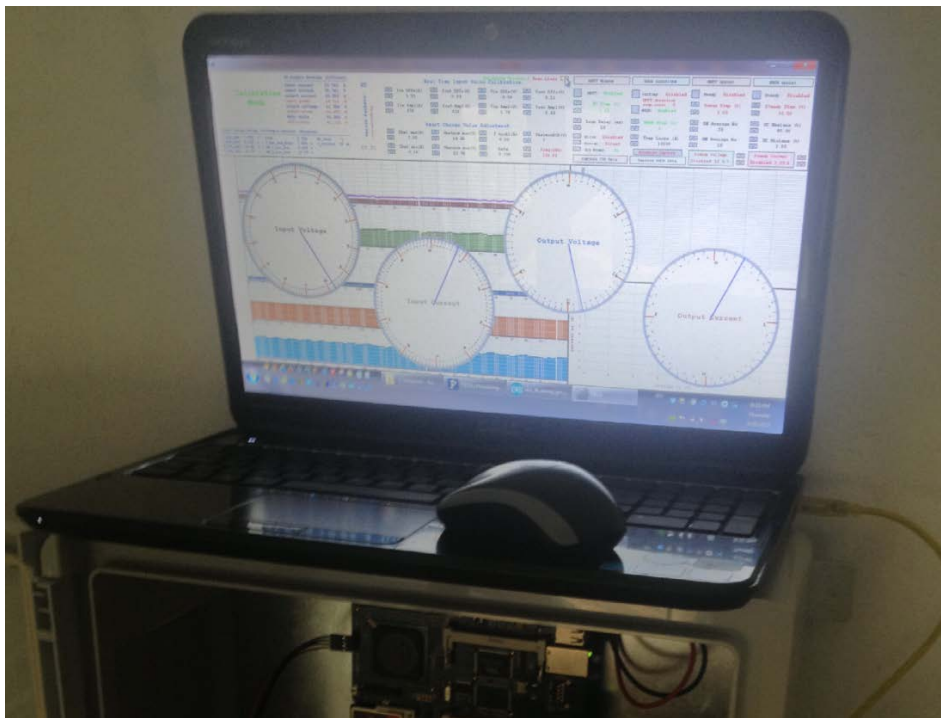


**Fig. 38.** Calibration of the voltage and current sensors of the DC-DC converter circuit.

The photograph of Fig. 38 displays the interface developed for debugging and testing purposes of the equipment during the development process. A pop-up overlay shows four cycles and a series of software buttons above these cycles. Of these buttons, 16 are in the upper center and refer to the group "Real Time Input Value Calibration" and undertake the role of properly calibrating the four measured values as sampled and represented in the

aforementioned circles. The calibration refers (from left to right) to the input voltage, the input current, the output voltage and the output current, respectively. The sampling rate varies while the lag (pause time) per code loop is being defined by the user. By default it has been set to 20 samples per second. Each one of the four circles holds two indices. This is a design choice that enhances the calibration accuracy. This is because the one represents an average value of 10 samples (which can also be altered by the user) that changes every half a second by default, so it is easy to read and the other one represents the instantaneous value, flickering fast enough to outline the range of noise of the respective channel under measurement. The photo was taken during the calibration process just right after installing the first power management system at the field (i.e. within the building that hosts the water-tank). The microcontroller was calibrated and its reported values for the input and output measurements of the voltage and current amplitude were satisfyingly accurate with a deviation of <1.0 % in all cases for the whole range of operation. The version of the interface shown in the photo was designed to be capable of operating in all similar platforms, such as Beagleboard RevC, Cubieboard, Intel Galileo Gen2, A10 Oliuxino Lime, IMX233, Aria G2, PCDuino and Raspberry Pi model B.

In order to ensure that the integrated circuits (ICs) of the load can receive data from the DC-DC converter when required, an appropriate code which transmits the battery voltage measurement via the I2C bus was added. Alongside the implementation of the data logging python code and the aforementioned connectivity tests, the addition of a Real Time Clock (RTC) and a flash memory logger were also added. This allows the independence of the DC-DC converter from a general PC device. It will also increase the robustness of the logging system, while allowing the communication with the external world at will, even in the event of a failure of the installed wireless network.

What followed next is the proper operation testing of the power generation and management system that was developed for the scenario that is met when a W/G is used to produce energy. The choice of using PV panels or W/G is determined by the system-level optimal design algorithm based on the meteorological conditions of the installation area. Despite the fact that most urban regions of Chania are located to areas with a low wind potential, still, the academic interest imposes the need of conducting concept-proof experiments using a suitable W/G.



**Fig. 39.** The W/G that was used in the experiments.

A picture of the W/G in action can be seen in Fig. 39. The W/G that was used in all these experiments has a rated power of 30 W and a maximum of 45 W and is a VAWT type (vertical axis wind generator) type. Although a W/G intuitively seems to be an improper RES to use in these areas, the experiments are still considered to be quite important since they can provide a quantitative estimation of the infeasibility margin. After conducting the experiments, it turns out that, as expected, the simulation results share common ground with what was expected in

practice. The DC-DC converter's MPPT algorithm performed very well but the power that was being generated while the W/G was placed in the natural environment was too little. For this reason the MPPT algorithm had to be artificially motivated to cover the full operational range of the W/G available by connecting its rotor to a properly configured test bench as shown in Fig. 40. The rotor of the wind generator was connected through a chain on a drill whose torque was manually regulated using a 500 W variac, as shown in Fig. 41.

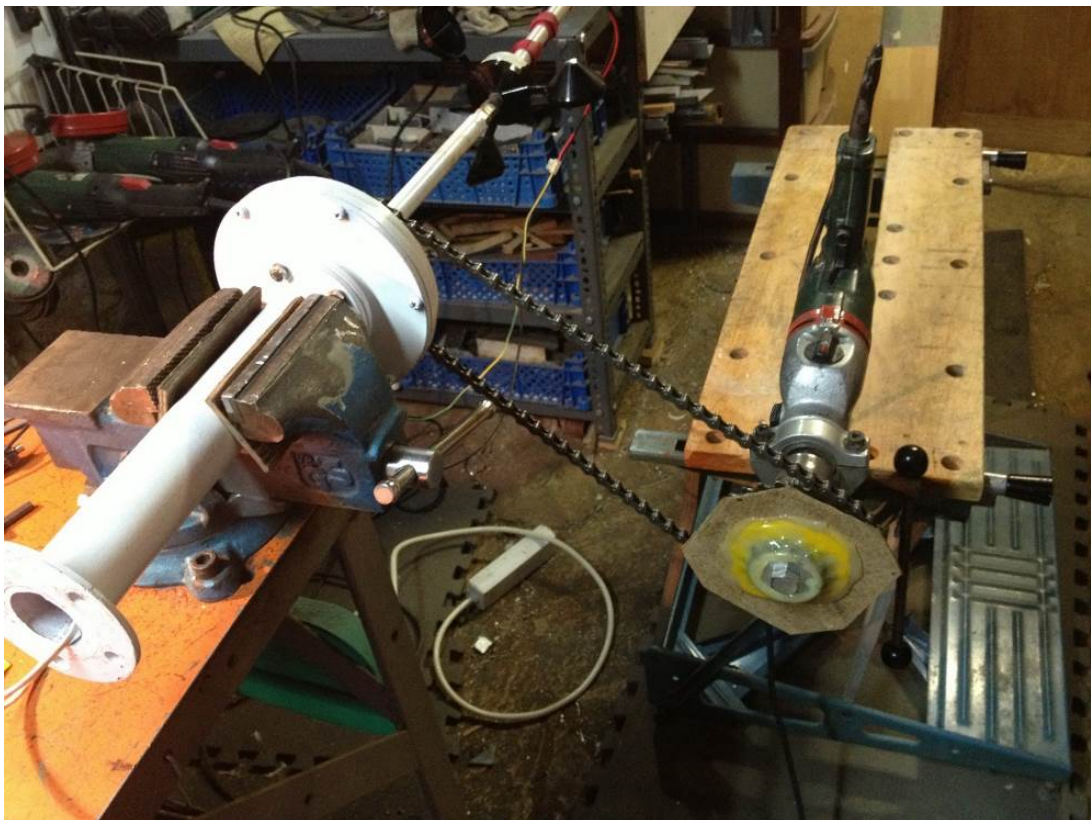


**Fig. 40.** The test bench employed for testing the operation of the W/G.

Fig. 42 is produced by the recorded data points that were collected when the setting of the maximum torque of the drill was in a very low level, thus allowing it to only reach a maximum of approximately 4 W of power generation. The data were collected in two phases that both lasted for about 10 minutes. The first one was with the duty cycle sweeping from 1 % to 99 %. These are the light blue points. The second one was when the MPPT P&O algorithm was active and the duty cycle was automatically reaching the values where the maximum power point was sensed to be (hill climbing effect).

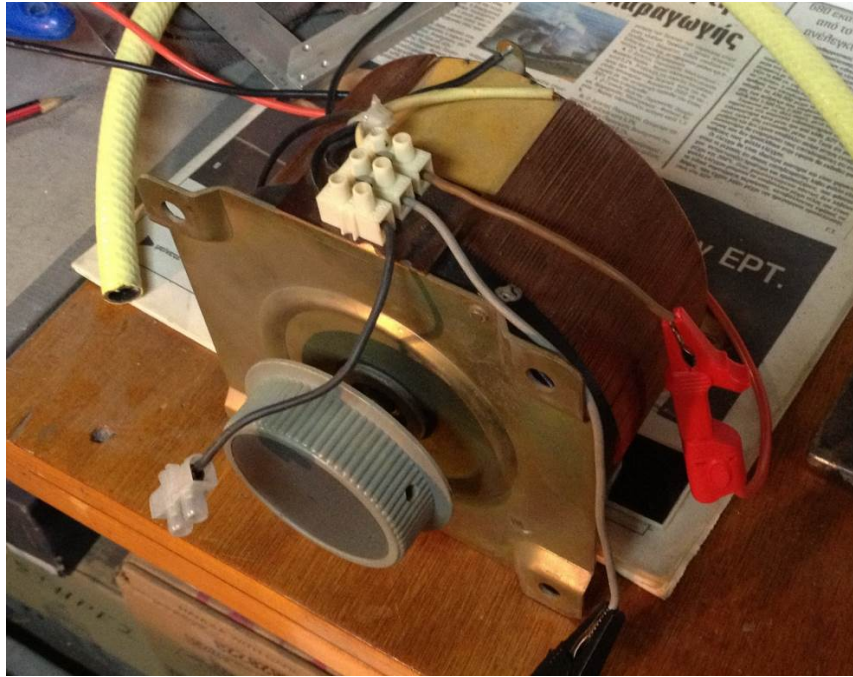


**Fig. 41.** The variac used to manually control the drill's torque.

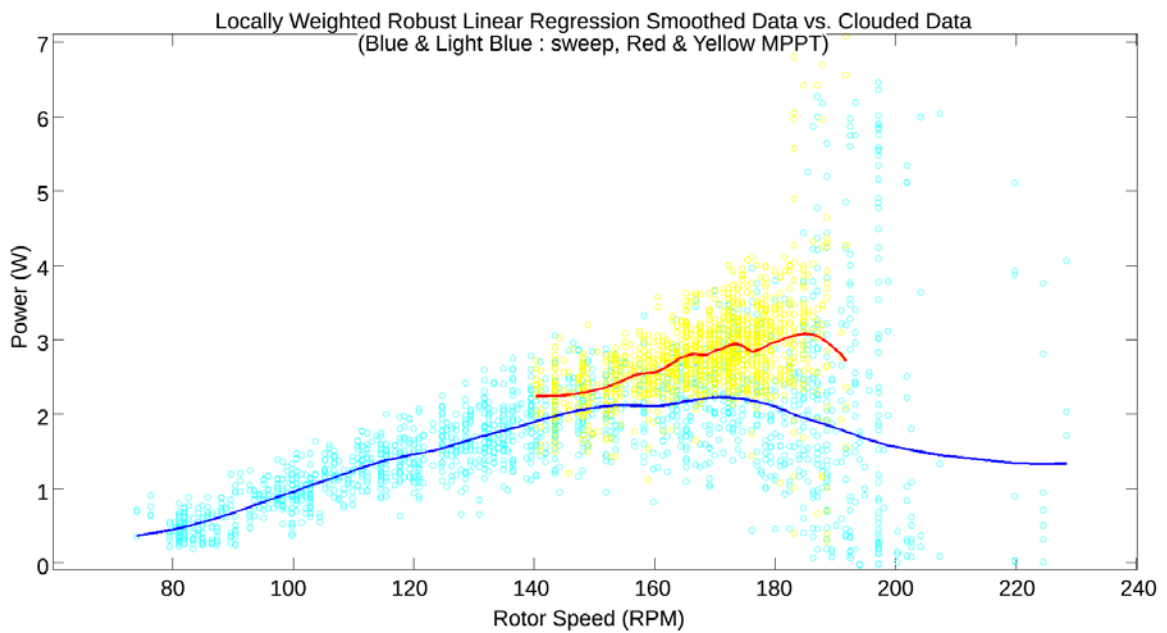


**Fig. 42.** The MATLAB plot that was produced by processing the data captured by the user-interface.

These are the yellow points. These are all the points that were collected and post-processed in the MATLAB environment in order to color them and to produce the two locally weighted linear regression lines as seen in the graph. The dark blue one shows the trend of the light blue

dots group and the red one shows the trend of the yellow dots group. By the shape and the relative position of the lines and the concentration of the yellow dots in relation to the light blue ones it is clearly shown that the MPPT algorithm pushes the duty cycle towards the neighborhood of the sensed maximum power point.

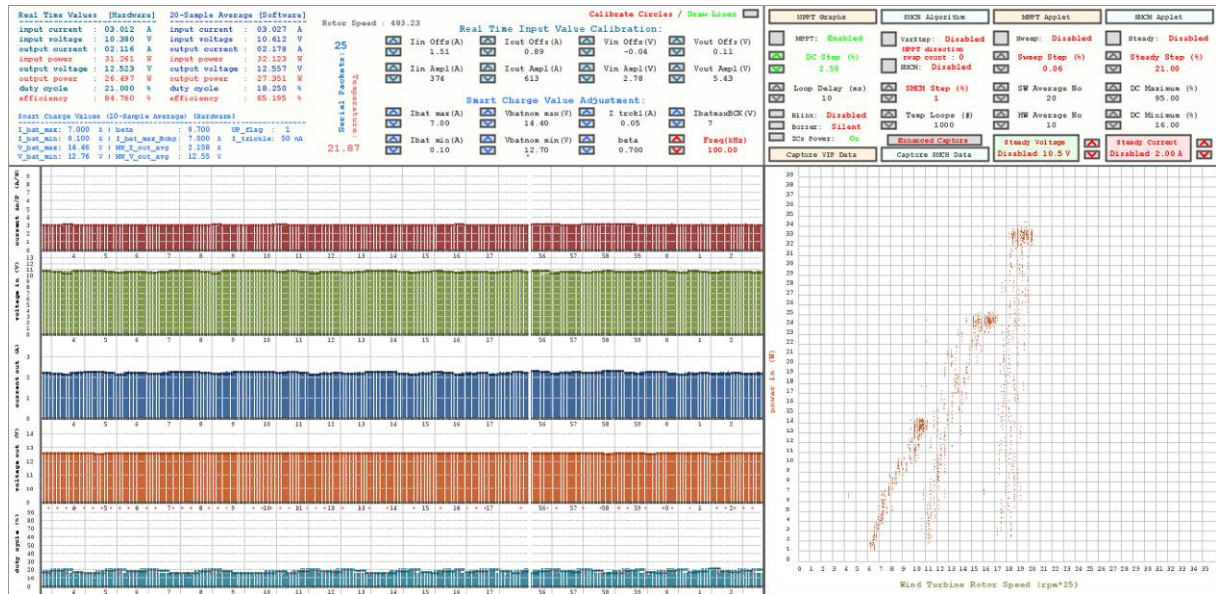


**Fig. 43.** The MPP is successfully reached for various fixed drill torque values (this experiment depicts three cases).

The screenshot confirming the proper operation of the power generation and management sub-system at high power levels (in relation to an order of magnitude less) can be seen in Fig. 43. It presents 3 distinct groups (clouds) of samples (dots). The experiment that produced those groups of samples was split in 3 phases. Each phase took about 20 minutes to complete. The only thing that was changing for phase to phase was the regulation of the drill's torque. Out of the 20 minutes that each phase took to complete, the first 10 minutes were dedicated to the sweeping of the duty cycle in the range from 1 % to 99 %, and the last 10 minutes were dedicated to the automated setting of the duty cycle according to the MPPT algorithm. As it is shown, in all 3 cases the algorithm successfully tracked the MPPT region as it can be clearly seen by the concentration of about half the dots in the upper part of each cloud.

## 5. Experimental results

### 5.1. Circuit-level optimization

The ICL7667 chip drives the MOSFET gate and the MOSFET opens and closes its source-to-drain channel in a manner depicted in Fig. 44. The most important of the information shown in that figure refers to the duty cycle, the amplitude and the rise/fall times of the pulse.

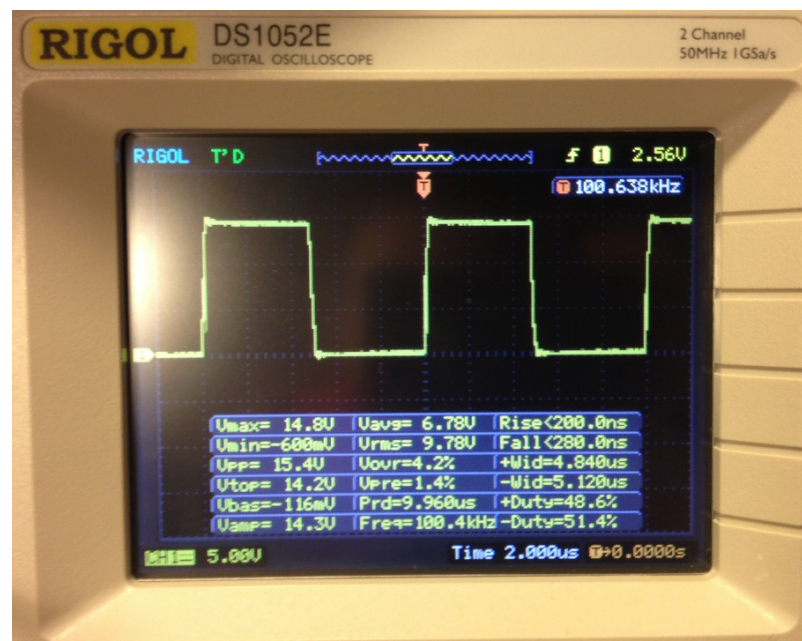


**Fig. 44.** Measuring the MOSFET driving pulse.

The efficiency of the system (which is over 83% for the first working prototype lacking any additional copper & solder wick) is presented in Fig. 45. The maximum efficiency of the DC-DC converter has been experimentally measured and, as noted, it exceeds 96 % at a power range of 80 W. Fig. 46 shows the corresponding snapshot of the interface that has been developed to automate this test procedure. The heat sinks that have been used in the PCBs all have the same heat dissipation capabilities. These heat sinks have been oversized to allow for an excellent heat dissipation even under strict conditions where the air flow is restricted. Similarly, proper care has been given to the design of the box vents hosting the board.



Fig. 45. An instance of the circuit and code experiments in action.

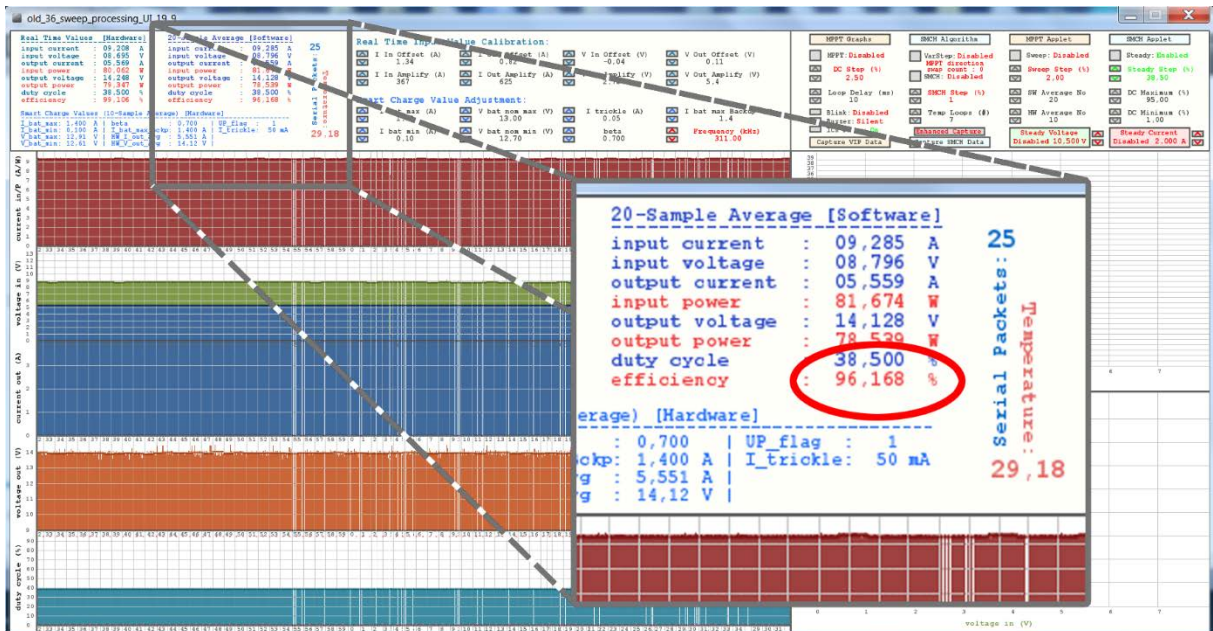
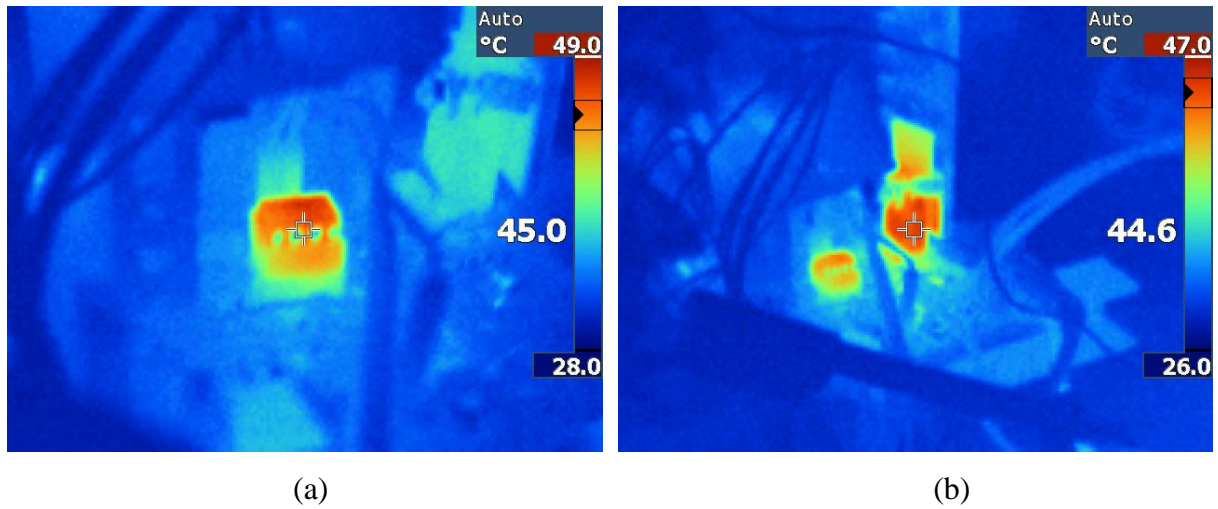
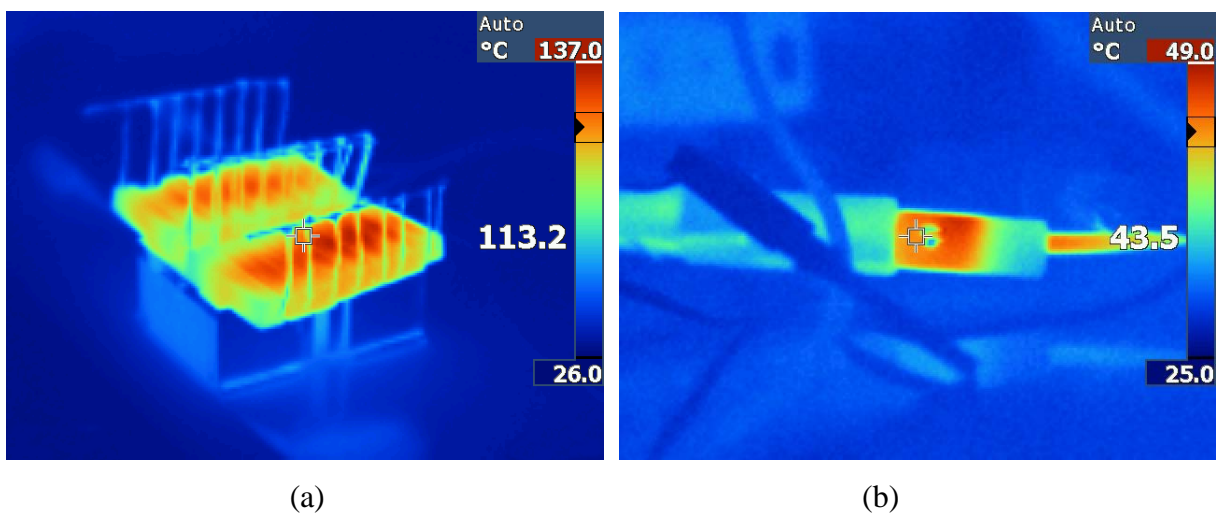


Fig. 46. Screenshot of the interface developed for monitoring and debugging the DC-DC converter's behavior. The maximum power efficiency achieved was over 96 % meeting the performance directive of the project's specifications.



**Fig. 47.** Thermal imaging of (a) the ICL7667 chip (b) the power diode of the converter.

Fig. 47 and Fig. 48 illustrate four thermal images aiming to highlight the distribution and diffusion of the heat generated by the various electronic components. Thermal imaging contributed as a tool by catering those needs and points to the extent necessary to stress out any imminent hardware failures that otherwise would appear only after long exposure time to milder environmental conditions. The first photo shows the chip that drives the power MOSFET. The second photo shows the temperature developed on the power diode.



**Fig. 48.** Thermal imaging of (a) the electric load and (b) the wiring connectors.

The photos were taken only after the DC-DC converter had ran at 45 W for 5 minutes. Fig. 48(a) shows the temperature developed on the connected load. Fig. 48(b) shows the temperature developed at the input power connector. As it turns out, the integrated circuit running the power MOSFET consumes less power than the maximum permitted according to the manufacturer, but still it gets heated more than the surrounding materials.

In order to experimentally evaluate the performance of the DC-DC converters, which are optimally designed using the proposed methodology, two identical prototype circuits were constructed using off-the-shelf components. The first one was developed by applying the optimal values of the design variables  $f_s$ ,  $MF_{Count}$ ,  $L$  and  $C_{out}$ , which have been derived by executing the proposed design optimization procedure for minimizing the power loss at maximum output power (i.e. Table 5), while the second one was constructed without applying a design optimization process. The difference between these two DC-DC converters were the inductance and switching frequency values which were employed. The optimized DC-DC converter was built using a 100  $\mu$ H inductor and a switching frequency of 128 kHz, so that the corresponding optimization results shown in Table 13 are approximated using the closest available values of the components. In contrast, a 390  $\mu$ H inductor and a 97 kHz switching frequency were employed in the non-optimized DC-DC converter. The voltage and current ripple constraints were also satisfied by the non-optimized DC-DC converter. The experimental prototype of a PV power-supplied Boost-type DC-DC converter was optimally designed using the proposed method. Each prototype DC-DC converter was then connected to a different battery bank comprising lead-acid batteries, which were all charged at the same voltage point of 12.41 V (measured under open-circuit conditions) and also power-supplying the same constant load of 3 W. Also, both DC-DC converters were receiving power from exactly the same type of solar panels standing side-by-side and facing towards the same direction. In order to maximize the power produced by the PV modules under the

continuously varying solar irradiation and ambient temperature conditions at the installation site, the control units of the DC-DC converters were programmed to execute the “Perturbation and Observation” Maximum Power Point Tracking (MPPT) process described in Section 4.1. The two WSN nodes were installed to operate simultaneously for a time period of four hours. The total energy produced by each PV array ( $E_{PV}$ ) as well as the total energy transferred to each battery bank ( $E_o$ ) respectively, during that test period, are presented in Table 13.

**Table 13.** Comparison of the optimized and non-optimized DC-DC converters in terms of the energy conversion efficiency.

	<i>Parameter</i>	<i>Value</i>
<i>Optimized DC-DC converter</i>	$E_{PV}$ (kWh)	19.86
	$E_o$ (kWh)	13.82
	$n_e$ (%)	69.6
<i>Non-optimized DC-DC converter</i>	$E_{PV}$ (kWh)	19.73
	$E_o$ (kWh)	13.02
	$n_e$ (%)	66.0

The experimentally measured time-series of the power, which was produced by the PV sources of the optimized and non-optimized DC-DC converters, respectively, are shown in Fig. 49. In order to compare the performance of the optimized and non-optimized DC-DC converters, without being affected by the deviation of the operational characteristics of the solar panels and batteries which were used in each of the two experimental prototypes, the normalized energy conversion efficiency has been calculated as follows:

$$n_e = \frac{E_o}{E_{PV}} \quad (17)$$

As shown in Table 13, the normalized energy conversion efficiency of the optimized DC-DC converter circuit is higher than that of the non-optimized one by 3.6 %, thus demonstrating the superiority offered by the proposed design optimization method.

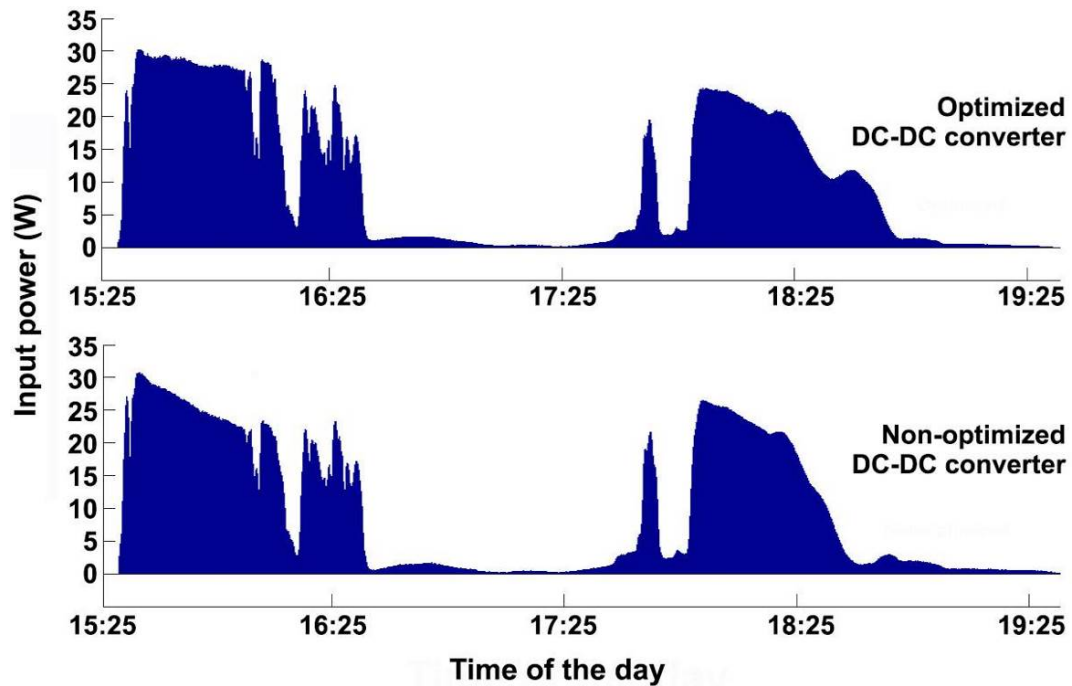


**Fig. 49.** The experimentally measured time-series of the power, which was produced by the PV sources of the optimized and non-optimized DC-DC converters, respectively, under MPPT conditions.

## 5.2. System-level optimization

Thereafter, what followed is the real-life experiments in the field which evaluate the maximum autonomy of the energy storage system. At first, these experiments were carried out without powering the batteries from the PV panels. So, in that context, after the tests that took place in "total darkness" the behavior of the PV panels was observed under partial cloudiness. The estimations from the original gathered data were confirmed by succeeding measurements (in the early October of the year 2014). These measurements are shown in another section of

this thesis on the graph of Fig. 50, where it is obvious that the voltage of the batteries during the night, i.e. while providing energy to the sensors and the load, does not fall below 12.35 V.

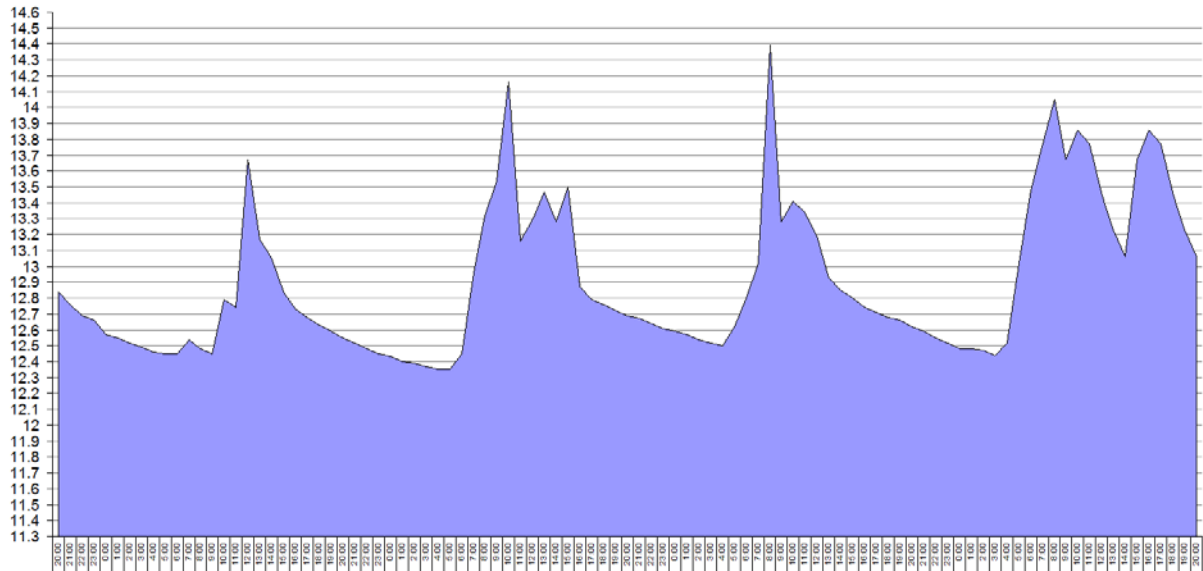


**Fig. 50.** Voltage variation of the batteries for four days under moderate cloudiness.

This revealed that the battery voltage decreases linearly during the day (about 0.4 V per 24 hours), which gives a very long margin of operation under cloudy weather. This margin is regarded to certainly be greater than the four days which was the original target, making the system reliable. Fig. 50 displays the corresponding data.

Similarly in another experiment, the resulting measured time-series of the power produced by the PV source, as well as the voltage and input/output power of the battery bank for a 48 h time interval, are shown in Fig. 51. In this case, the battery is discharged during the time intervals that PV-generated energy is not available (indicated by the negative values of the battery power in the figure), in order to provide the power required by the electric load. However, the maximum permissible depth of discharge limit is never exceeded, thus guaranteeing the reliable operation of the power-supply system.

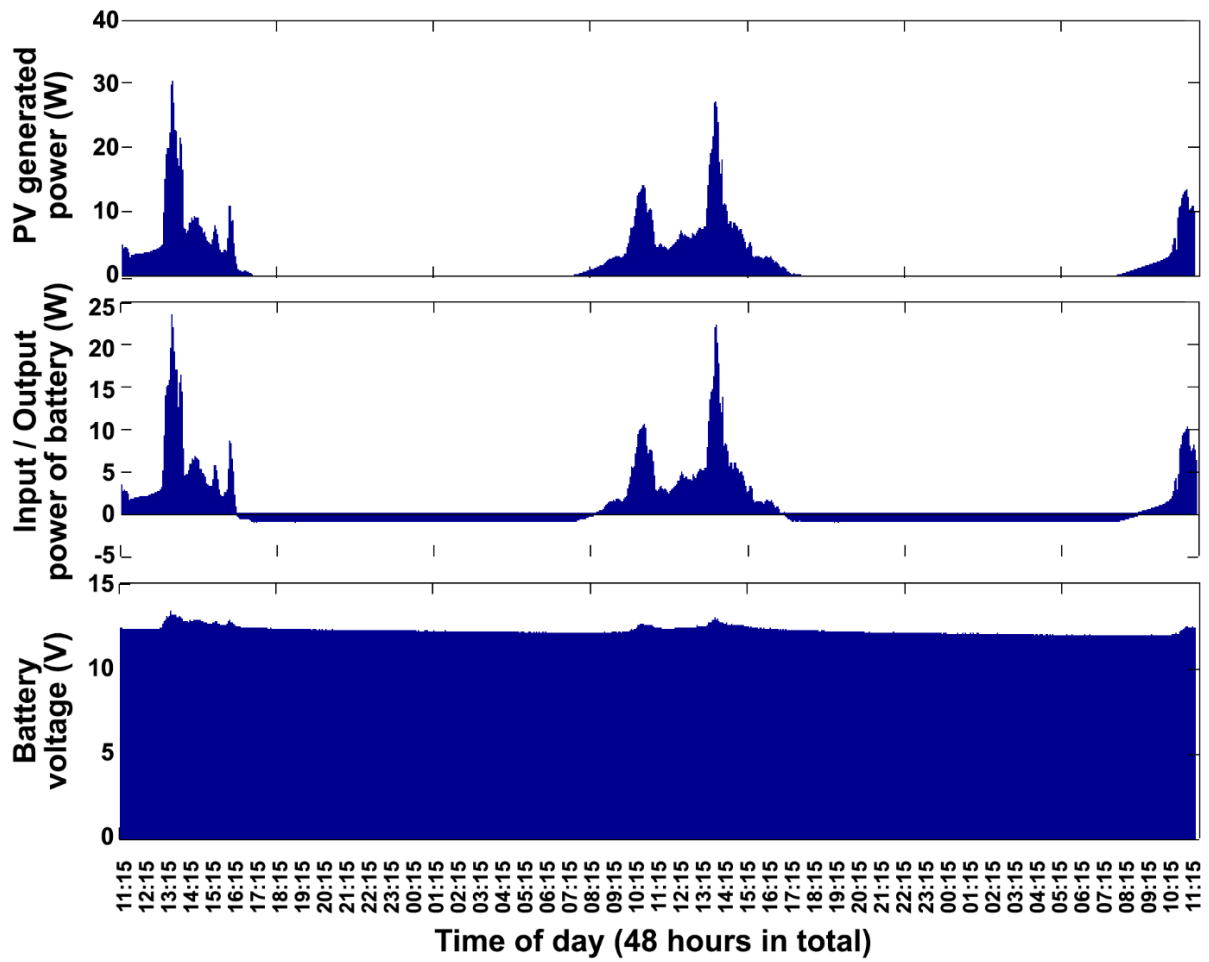


**Fig. 51.** The experimentally measured time-series of the power produced by the PV source, as well as the voltage and input/output power of the battery bank.

## 6. Conclusion

WSNs are widely installed for monitoring multiple parameters of interest over distributed areas in the environment, buildings and industries. Since they are frequently installed in geographically remote areas, the WSN nodes are power-supplied by RES. Thus, a DC-DC power converter is employed for interfacing the generated energy to a battery bank and the electric load of the WSN node. The design of the WSN node power-supply system can have a great impact on the total cost of the WSN node and affect its reliability.

In this thesis, a novel method for performing circuit-level optimization of a PV power-supplied Boost-type DC-DC power converter, which is employed in a WSN node, has been presented. Using the proposed technique enables to calculate the optimal switching frequency and values of the components comprising the circuit of the DC-DC converter, such that either the power loss at nominal output power, or the total power loss during the year, or the LCOE, are alternatively minimized. Also, towards the same direction, a technique for the optimal design of a WSN node power-supply system, which is based on the use of RES, has been presented. This technique enables to derive the optimal type of RES, storage and charger characteristics, which is mostly suitable for the installation site under consideration according to the prevailing meteorological conditions. The corresponding configuration of the power-supply system will result in the minimization of the total lifetime cost of the WSN node, while simultaneously guaranteeing that the data-acquisition equipment is uninterruptedly power-supplied during the year. Both simulation and experimental results have been presented, which, compared to the respective non-optimized DC-DC converter and power-supply system structures, demonstrate the performance superiority of the proposed methods.

Future work may include the long-term experimental testing of the optimized DC-DC converters and the overall power-supply system, in order to evaluate their performance in terms of reliability, annual energy production and total power loss (of the charger) during the year.

## 7. References

1. K. Shafiullah, K.P. Al-Saki and A.A.Nabil, "Wireless Sensor Networks - Current Status and Future Trends," CRC Press, 2012.
2. J. Xiaofan, J. Polastre and D. Culler, "Perpetual environmentally powered sensor networks," 4<sup>th</sup> International Symposium on Information Processing in Sensor Networks, pp.463-468, 2005.
3. S. K. K. Ng, J. Zhong and J. W. M. Cheng, "Probabilistic optimal sizing of stand-alone PV systems with modeling of variable solar radiation and load demand," IEEE Power and Energy Society General Meeting, pp. 1-7, 2012.
4. X. Daming and K. Longyun, "Multi-criteria Optimization of Off-grid Renewable Energy Systems," 35<sup>th</sup> International Telecommunications Energy Conference (INTELEC), pp. 1-5, 2013.
5. K. Deb, "Multi-Objective Optimization using Evolutionary Algorithms," Chichester, England, John Wiley & Sons, 2001.
6. V. Raviprasad and R. K. Singh, "Optimal sizing of PV array for critical load with parallel redundant architecture using GA," 1<sup>st</sup> International Conference on Automation, Control, Energy and Systems (ACES), pp. 1-7, 2014.
7. L. Zhongshi, Z. Wei and Y. Hongxing, "One Novel Optimum Sizing Method for Solar Lighting System by Using Genetic Algorithm," International Conference on Energy and Environment Technology, vol. 1, pp. 225-228, 2009.
8. S. Jimenez-Fernandez, S. Salcedo-Sanz, G. Gomez-Prada, L. Carro-Calvo, A. Portilla-Figueras and J. Maellas-Benito, "Sizing a hybrid photovoltaic-hydrogen system for remote telecommunication stand-alone facilities using evolutionary algorithms," 11<sup>th</sup> International Conference on Intelligent Systems Design and Applications (ISDA), pp. 1271-1275, 2011.

9. A. A. Al-Shamma'a and K. E. Addoweesh, "Optimum sizing of hybrid PV/wind/battery/diesel system considering wind turbine parameters using Genetic Algorithm," IEEE International Conference on Power and Energy (PECon), pp. 121-126, 2012.
10. O. H. Mohammed, Y. Amirat, M. Benbouzid and A. A. Elbaset, "Optimal design of a PV/fuel cell hybrid power system for the city of Brest in France," International Conference on Green Energy, pp. 119-123, 2014.
11. M. Kolhe, K. M. I. U. Ranaweera and A. G. B. S. Gunawardana, "Techno-economic optimum sizing of hybrid renewable energy system," 39<sup>th</sup> Annual Conference of the IEEE Industrial Electronics Society (IECON), pp. 1898-1903, 2013.
12. F. Z. Kadda, S. Zouggar, M. El hafyani and A. Rabhi, "Contribution to the optimization of the electrical energy production from a Hybrid Renewable Energy system," 5<sup>th</sup> International Renewable Energy Congress (IREC), pp. 1-6, 2014.
13. HOMER software, <http://www.homerenergy.com/>.
14. A. Mohamed and T. Khatib, "Optimal sizing of a PV/wind/diesel hybrid energy system for Malaysia," IEEE International Conference on Industrial Technology (ICIT), pp. 752-757, 2013.
15. I. Tegani, A. Aboubou, M. Becherif, M. Y. Ayad, O. Kraa, M. Bahri and O. Akhrif, "Optimal sizing study of hybrid wind/PV/diesel power generation unit using genetic algorithm," 4<sup>th</sup> International Conference on Power Engineering, Energy and Electrical Drives (POWERENG), pp. 134-140, 2013.
16. V. Kalkhambkar, R. Kumar and R. Bhakar, "Optimal sizing of PV-battery for loss reduction and intermittency mitigation," Recent Advances and Innovations in Engineering (ICRAIE), pp. 1-6, 2014.

17. A. T. D. Perera, R. A. Attalage and K. K. C. K. Perera, "Optimal design of a grid connected hybrid electrical energy system using evolutionary computation," 8<sup>th</sup> IEEE International Conference on Industrial and Information Systems (ICIIS), pp. 12-17, 2013.
18. A. Arabali, M. Ghofrani, M. Etezadi-Amoli, M. S. Fadali and Y. Baghzouz, "Genetic-Algorithm-Based Optimization Approach for Energy Management," IEEE Transactions on Power Delivery, vol. 28, no. 1, pp. 162-170, 2013.
19. M. B. Shadmand and R. S. Balog, "Multi-Objective Optimization and Design of Photovoltaic-Wind Hybrid System for Community Smart DC Microgrid," IEEE Transactions on Smart Grid, vol. 5, no. 5, pp. 2635-2643, 2014.
20. M. Kolhe, "Techno-Economic Optimum Sizing of a Stand-Alone Solar Photovoltaic System," IEEE Transactions on Energy Conversion, vol. 24, no. 2, pp. 511-519, 2009.
21. F. Wang, W. Shen, D. Boroyevich, S. Ragon, V. Stefanovic and M. Arpilliere, "Design optimization of industrial motor drive power stage using Genetic Algorithms," CES/IEEE 5<sup>th</sup> International Power Electronics and Motion Control Conference (IPEMC), vol. 1, pp. 1-5, 2006.
22. C. Larouci, J. P. Didier, A. Aldebert, O. Bouquet, A. Prost and J. Vauchel, "Optimal design of a synchronous DC-DC converter using analytical models and a dedicated optimization tool," 29<sup>th</sup> Annual Conference of the IEEE Industrial Electronics Society (IECON), vol. 2, pp. 1623-1628, 2003.
23. H. Helali, D. Bergogne, H. Morel and J. B. H. Slama, "Power converter design methodology: uses of multiple objective techniques for optimization of a (42/14V) buck converter," 4<sup>th</sup> International Conference on Integrated Power Systems (CIPS), pp.1-5, 2006.

24. K. Ejjabraoui, C. Larouci, P. Lefranc and C. Marchand, "A new pre-sizing approach of DC-DC converters, application to a boost converter for the automotive domain," 35<sup>th</sup> Annual Conference of the IEEE Industrial Electronics Society (IECON), pp. 3767-3772, 2009.
25. X. Ma and R. L. Liu, "Reactive power optimization in power system based on improved niche genetic algorithm," International Conference on Computer Design and Applications (ICCCA), vol. 3, pp. 413-416, 2010.
26. K. Rayudu, A. Jayalaxmi, G. Yesuratnam and Y. D. Kumar, "Multi objective comparison of GA and LP techniques for generator reactive power optimization," IEEE 5<sup>th</sup> Power India Conference, pp.1-5, 2012.
27. R. Lukomski and K. Wilkosz, "Optimization of reactive power flow in a power system for different criteria: stability problems," 8<sup>th</sup> International Symposium on Advanced Topics in Electrical Engineering (ATEE), pp. 1-6, 2013.
28. S. Chen, P. Li, D. Brady and B. Lehman, "Determining the optimum grid-connected photovoltaic inverter size," Solar Energy, vol. 87, pp. 96-116, 2013.
29. J. Luoma, J. Kleissl and K. Murray, "Optimal inverter sizing considering cloud enhancement," Solar Energy, vol. 86, pp. 421-429, 2012.
30. E. Koutroulis, F. Blaabjerg, "Design optimization of transformerless grid-connected PV inverters including reliability", IEEE Transactions on Power Electronics, Vol. 28, No. 1, pp. 325-335, 2013.
31. H. Helali, D. Bergogne, J.B.H. Slama, H. Morel, P. Bevilacqua, B. Allard and O. Brevet, "Power converter's optimisation and design. Discrete cost function with genetic based algorithms," 2005 European Conference on Power Electronics and Applications, pp. 1-7, 2005.

32. L. Jourdan, J-L Schanen, J. Roudet, M. Bensaïed, K. Segueni, "Design methodology for non insulated DC-DC converter: application to 42V-14V "Powernet"," IEEE 33<sup>rd</sup> Annual Power Electronics Specialists Conference, vol. 4, pp. 1679-1684, 2002.
33. S. Busquets-Monge, G. Soremekun, E. Hefiz, C. Crebier, S. Ragon, D. Boroyevich, Z. Gurdal, M. Arpilliere and D. K. Lindner, "Power converter design optimization," IEEE Industry Applications Magazine, vol. 10, no. 1, pp 32-38, 2004.
34. E. Koutroulis, F. Blaabjerg, "Methodology for the optimal design of transformerless grid-connected PV inverters", IET Power Electronics, Vol. 5, No. 8, pp. 1491-1499, 2012.
35. E. Koutroulis and K. Kalaitzakis, "Novel battery charging regulation system for photovoltaic applications," IEE Proceedings - Electric Power Applications, vol. 151, no. 2, pp. 191-197, 2004.
36. G. M. Dousoky, E. M. Ahmed and M. Shoyama, "Current-sensorless MPPT with DC-DC boost converter for photovoltaic battery chargers," 2012 IEEE Energy Conversion Congress and Exposition (ECCE), pp. 1607-1614, 2012.
37. A. Huang, "Infineon OptiMOS Power MOSFET Datasheet Explanation," Infineon Application Notes, 2013, Web.
38. Dr. D. Graovac, M. Pürschel and A. Kiep, "MOSFET Power Losses Calculation Using the DataSheet Parameters," Infineon Application Notes, 2006, Web.
39. T. Eichhorn, "Boost Converter Efficiency Through Accurate Calculations," Cours Et TD Pour 2013/2014 Et Avant, Power Electronics Technology, 2008, Web.
40. K. H. Billings and T. Morey, "Switchmode Power Supply Handbook," New York: McGraw-Hill, 2011, Web.
41. R. W. Erickson and D. Maksimovic, "Fundamentals of Power Electronics," 2nd ed., Springer, 2001, Web.

42. "Coilcraft DC-DC Converter Design Center." Coilcraft DC-DC Converter Design Center. N.p., n.d. Web.
43. "Determining Inductor Power Losses Document," 486 pages, EDUCYPEDIA - The Educational Encyclopedia, Coilcraft, 2009, Web.
44. "Magnetics," Transformer Design with Ferrite Cores, Web.
45. R. Yuancheng, X. Ming, J. Zhou and F. C. Lee, "Analytical loss model of power MOSFET," IEEE Transactions on Power Electronics, vol. 21, no. 2, pp. 310-319, 2006.
46. X. Yu and P. Yeaman, "Temperature-related MOSFET power loss modeling and optimization for DC-DC converter," 28<sup>th</sup> Annual IEEE Applied Power Electronics Conference and Exposition (APEC), pp. 2788-2792, 2013.
47. K. Billings, H. Keith and T. Morey, "Switchmode Power Supply Handbook", McGraw-Hill, 3<sup>rd</sup> ed., 2011.
48. L. Jinjun, T. G. Wilson, R. C. Wong, R. Wunderlich and F. C. Lee, "A method for inductor core loss estimation in power factor correction applications," 17<sup>th</sup> Annual IEEE Applied Power Electronics Conference and Exposition (APEC), vol. 1, pp. 439-445, 2002.
49. W. A. Roshen, "A practical, accurate and very general core loss model for nonsinusoidal waveforms," IEEE Transactions on Power Electronics, vol. 22, no. 1, pp. 30-40, 2007.
50. J. Muhlethaler, J. Biela, J. W. Kolar and A. Ecklebe, "Improved core loss calculation for magnetic components employed in power electronic system," 26<sup>th</sup> Annual IEEE Applied Power Electronics Conference and Exposition (APEC), pp. 1729-1736, 2011.
51. E. Koutroulis, K. Kalaitzakis and N. C. Voulgaris, "Development of a microcontroller-based, photovoltaic maximum power point tracking control system," IEEE Transactions on Power Electronics, vol. 16, no. 1, pp. 46-54, 2001.

52. E. Koutroulis and K. Kalaitzakis, "Design of a maximum power tracking system for wind-energy-conversion applications," *IEEE Transactions on Industrial Electronics*, vol. 53, no. 2, pp. 486-494, 2006.
53. T. Eswam and P. L. Chapman, "Comparison of photovoltaic array maximum power point tracking techniques," *IEEE Trans. on Energy Conversion*, vol. 22(2), pp. 439-449, 2007.
54. R. Faranda and S. Leva, "Energy comparison of MPPT techniques for PV systems," *WSEAS transactions on power systems*, vol. 3(6), pp. 446-455, 2008.
55. Z. Michalewicz, "Genetic Algorithms + Data Structures = Evolution Programs," 2<sup>nd</sup> ed., New York, Springer-Verlag, 1994.
56. R. Vepa, "Dynamic Modeling, Simulation and Control of Energy Generation," *Lecture Notes in Energy*, Springer, 2013.
57. E. Lorenzo, "Solar Electricity-Engineering of Photovoltaic Systems," 1<sup>st</sup> ed., PROGNSA, 1994.